



Cite this: *Phys. Chem. Chem. Phys.*,
2021, 23, 7615

Received 19th October 2020,
Accepted 1st December 2020

DOI: 10.1039/d0cp05476c

rsc.li/pccp

Grazing incidence fast atom diffraction, similarities and differences with thermal energy atom scattering (TEAS)

Maxime Debiossac, † Peng Pan and Philippe Roncin *

Grazing incidence fast atom diffraction (GIFAD) at surfaces has made rapid progress and has established itself as a surface analysis tool where effective energy E_{\perp} of the motion towards the surface is in the same range as that in thermal energy atom scattering (TEAS). To better compare the properties of both techniques, we use the diffraction patterns of helium and neon atoms impinging on a LiF (001) surface as a model system. E -Scan, θ -scan, and ϕ -scan are presented where the primary beam energy E is varied between a few hundred eV up to five keV, the angle of incidence θ_i between 0.2 and 2° and the azimuthal angle ϕ_i around 360° . The resulting diffraction charts are analyzed in terms of high and low values of effective energy E_{\perp} . The former provides high resolution at the positions of the surface atoms and the attached repulsive interaction potentials while the second is sensitive to the attractive forces towards the surface. The recent progress of inelastic diffraction is briefly presented.

1 Introduction, grazing incidence

This paper is dedicated to grazing incidence fast atom diffraction (GIFAD) at surfaces. This new diffraction technique has strong similarities with thermal energy atom scattering (TEAS or HAS) developed in the '70s by Toennies *et al.*,¹ Lapujoulade *et al.*,² Mattera *et al.*,³ Rieder *et al.*⁴ and others as reviewed in several papers.^{5–10} As part of a special issue with several contributions on atomic diffraction, we refer the readers to these contributions for a more in depth discussion on the current status of TEAS. To better illustrate the specificity of GIFAD, we focus here on the extensively studied model system of helium and neon atoms impinging on a LiF (001) surface.

Grazing incidence fast atom diffraction was discovered fifteen years ago^{11–13} but could have been observed much earlier because it requires only a comparatively simple setup:¹⁴ a commercial keV ion source, a custom neutralization cell and a position-sensitive detector. These became available in the 80's with the advent of micro-channel plates and investigations of surfaces by ions at grazing incidences was already well developed by Kimura *et al.*¹⁵ and Winter *et al.*¹⁰ Diffraction of fast atoms under grazing incidence was predicted by Andreev¹⁶ a few years before its first observation. However, the paper did not attract much attention, probably because it

was firmly believed that inelastic processes would lead to decoherence, washing out diffraction features.

Soon after the first observation, it was realized that GIFAD has strong similarities with reflection high-energy electron diffraction (RHEED see Table 3 for abbreviations)¹⁷ as well as with thermal energy atom scattering. It was immediately noted that the fast motion along the low index direction, taken here as the x axis, is strongly decoupled^{11,13} from the much slower motion in the perpendicular (y,z) plane (see Fig. 1). Here, $\vec{k}_i(k_{ix}, k_{iy}, k_{iz})$ and $\vec{k}_f(k_{fx}, k_{fy}, k_{ fz})$ represent the components of the projectile wave-vector respectively before and after scattering on the surface. The angle between the projectile wave-vector \vec{k} and its projection on the surface ($k_x, k_y, 0$) is the polar angle θ while the angle between this projection and the low index

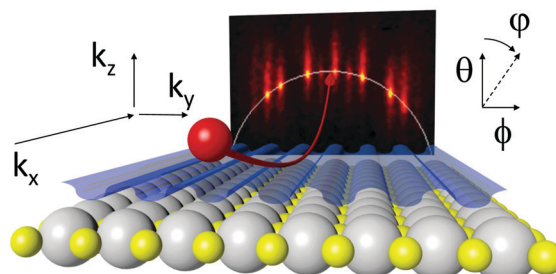


Fig. 1 Illustration of a GIFAD experiment. The primary beam of Ne neutral atoms bounces a few Å above the crystal surface. When the beam is aligned with a low index direction, it is diffracted by the well-aligned rows of surface atoms before being collected on an imaging detector.

Université Paris-Saclay, CNRS, Institut des Sciences Moléculaires d'Orsay (ISMO), 91405 Orsay, France. E-mail: philippe.roncin@u-psud.fr

† Present address: University of Vienna, Faculty of Physics, VCQ, Boltzmanngasse 5, A-1090 Vienna, Austria.

Table 1 Comparison of LEED, TEAS and their grazing incidence equivalent RHEED and GIFAD. Here E is the total kinetic energy, θ_i is the polar incidence angle and E_{\perp} , λ_{\perp} are the perpendicular energy and wavelength

	Probe	E (eV)	θ_i ($^{\circ}$)	E_{\perp} (meV)	λ_{\perp} (\AA)
GIFAD	He	100–5000	<1	1–1000	0.1–5
TEAS	He	10^{-3} – 10^{-1}	10–170	1–100	0.5–5
RHEED	e^-	10^4 – 10^5	<5.0	10^3 – 10^5	0.5–10
LEED	e^-	50–100	90	5×10^4 – 10^5	~1

direction $(1,0,0)$ is the azimuthal angle ϕ . The angle between the two components k_y and k_z is called the deflection angle φ . The perpendicular energy $E_{\perp} = \hbar^2(k_{iy}^2 + k_{iz}^2)/2m_p$ of the motion in the (y,z) plane corresponds to a particle of mass m_p evolving in the axially averaged interaction potential $V_{2D}(y,z)$ (see eqn (1)). In GIFAD, the perpendicular energy E_{\perp} can be tuned from a few meV to several eV, by sweeping for instance the incidence angle, covering the energy range used in standard TEAS experiments. From the geometrical point of view, GIFAD is to TEAS what RHEED is to LEED as summarized in Table 1.

The decoupling from the slow to the fast motion, called axial surface channeling approximation (ASCA), has been investigated in detail.^{11,18–20} Through this review evidence that the low index direction is indeed a genuine reference axis for the scattering will be presented, supporting the validity of ASCA.

The paper is organized as follows: we present a brief description of the specific grazing geometry of fast atom diffraction (Section 2), before covering a standard GIFAD experimental setup (Section 3). Section 4 then focuses on theoretical tools to analyse the GIFAD diffraction patterns. In Section 5, we explain the differences between elastic and inelastic diffraction based on experimental data. Elastic diffraction is then treated in detail in Section 6 using θ -scan, ϕ -scan, and E -scan, with special attention on the sensitivity to surface topology and attractive forces. Finally, inelastic diffraction is discussed in light of a quantum binary collision model in Section 7.

2 Projectile trajectory

The large kinetic energy (hundreds of eV) used in GIFAD provides a very high detection efficiency compatible with the use of a position sensitive detector. This allows for the full diffraction image to be recorded at once and within seconds. However, the fundamental difference with TEAS is not the energy but the grazing scattering geometry, causing successive interactions with many atoms of the surface. The coherent contribution of the sum of all these small successive interactions produces a significant deflection of the incoming beam along the z motion. Fig. 2a represents the projectile trajectory $z(x)$ of a 1 keV helium atom impinging at 1° incidence on top of an atomic row of F^- ions of a LiF surface oriented along the $\langle 110 \rangle$ direction. The interaction with the individual surface atoms is very well localized as illustrated with the peaks on the blue and red curves representing the acceleration in the vertical and horizontal directions, respectively. These also represent the force

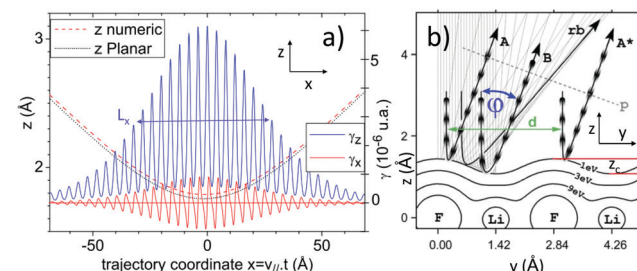


Fig. 2 (a) Classical trajectory $z(x)$ of a 1 keV ${}^4\text{He}$ atom impinging at $\theta_i = 1^\circ$ incidence along the $\langle 110 \rangle$ direction on the LiF (001) surface.²¹ The full blue and red curves represent the vertical and horizontal components of the acceleration vector. The red dashed line is calculated with the full 3D potential $V_{3D}(\vec{r})$ and is almost identical to the analytic one calculated with the mean repulsive planar potential, $V_{1D}(z)$ in eqn (1). (b) Projectile trajectories $z(y)$ and equipotential lines of the 2D interaction potential $V_{2D}(y,z)$ relevant for the scattering in the (y,z) plane (taken from ref. 22).

and momentum exchange between the helium projectile and the surface atoms. Along the z direction, all peaks are positive, pushing the projectile away from the surface while along x the projectile is first slowed down when approaching a surface atom and is accelerated when leaving resulting in a vanishingly small integral as predicted by Henkel *et al.*²³ and observed by Farias *et al.*²⁴ in TEAS at grazing incidence. The envelope of these sharp peaks possesses a quasi-Gaussian envelope with a well defined standard deviation. This width represents the mean length of the interaction and, neglecting the attractive forces, it scales with the inverse of the angle of incidence θ_i .^{21,25} The more grazing the angle of incidence, the broader the interaction curves and also the weaker the amplitude because the integral is proportional to twice the initial momentum towards the surface to ensure specular reflection. In Section 7, all the inelastic effects specific to GIFAD will be interpreted as due to these multiple gentle collisions. In the (y,z) plane (Fig. 2b), from ref. 22, projectile trajectories resemble the one observed from standard TEAS collisions with a slow projectile incoming around 90° ($\varphi = 0^\circ$) above the surface and bouncing on the surface atoms while in GIFAD, the bumps in the (y,z) plane correspond to atomic rows.

3 A GIFAD setup

Fig. 3 shows a schematic drawing of a GIFAD setup with two opposite arms connected to the main UHV chamber hosting the crystal surface. The left-hand side is dedicated to neutral beam production while the right-hand-side is for the detection. Both are essentially long tubes leaving full access to the 2π volume above the surface. For an incidence angle θ_i and an incidence azimuthal angle ϕ_i , $\vec{k}_i = k_i(\cos \theta_i \cos \phi_i, \cos \theta_i \sin \phi_i, \sin \theta_i) \approx k_i(1, \phi_i, \theta_i)$.

3.1 Beam and surface properties

Neutral atoms are produced by resonant charge exchange into a 2 cm long cell filled with helium at a pressure of about 10^{-3} mbar. With electron capture cross-sections on the order of 10^{-15} cm 2 , this is enough to ensure that approximately 10%

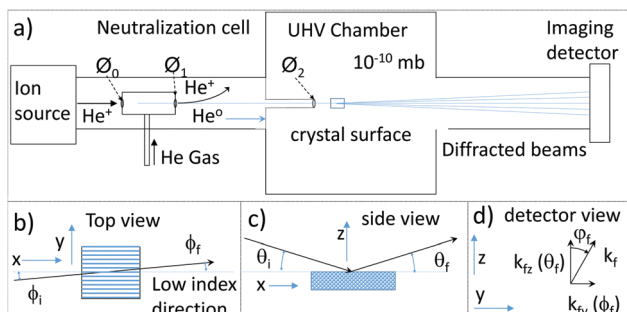


Fig. 3 Scheme of the experimental setup. (a) He⁺ ions, extracted from the ion source at keV energy, are converted into neutral He⁰ atoms after resonant charge exchange into a gas cell. The neutral beam is collimated by two diaphragms Ø₀ and Ø₁ to control its angular spread $\delta\theta$. After reflection on the crystal surface in the UHV chamber, the diffracted beams are collected on an imaging detector ≈ 1 m downstream. (b–d) are schematic views of the scattering geometry and define the polar and azimuthal incidence angles θ_i and ϕ_i , the lateral deflection angle ϕ_f , the polar exit angle θ_f and the deflection angle φ_f .

of ions are converted into neutral atoms with almost the same energy and divergence angle as the ion beam. Two small diaphragms of diameter Ø₀ and Ø₁ are installed at both ends of the neutralization cell to reduce leaks from the helium gas. The diaphragm Ø₁ also defines the source size of the atomic beam. The angular spread $\delta\theta$ of the atomic beam is set by a second diaphragm Ø₂ located at a distance L downstream so that the angular resolution is $\delta\theta \simeq (\mathcal{O}_1 + \mathcal{O}_2)/4L$.

In order to resolve diffraction, the angular resolution should be less than the Bragg angle associated with the surface, $\phi_B \simeq G_y/k$ where k is the projectile wave number and $G_y = 2\pi/a_y$ is the reciprocal lattice vector associated with the periodic arrangement a_y of the atomic rows. G_y is typically less than a few Å⁻¹ while a 1 keV He atom wave number k is larger than one thousand Å⁻¹. This translates to diaphragm sizes between 50 and 10 μm to resolve the Bragg angle. It corresponds to a transverse momentum spread $\delta k_{\perp} = k\delta\theta$ and a transverse beam coherence of δ_y or $\delta_z \simeq \delta k_{\perp}^{-1}$ defined by the Heisenberg uncertainty relationship which is usually limited below 10–20 Å. This is much less than with TEAS⁴ which can reach 100 Å and this limits the ability of GIFAD to distinguish large lattice cells. However, due to the grazing incidence angle $\theta_i \approx 1^\circ$ used in GIFAD, the length coherently illuminated along the x direction is $\theta_i^{-1} \sim 100$ times larger. So far, only Busch *et al.*¹⁸ have succeeded in partly exploiting this longitudinal sensitivity; this aspect was also discussed as a contribution to the scattering line-profile in ref. 26 and 27. With the observation of elastic diffraction spots having the same size as the primary beam, as visible in Fig. 4a, the asymmetry between the longitudinal and transverse coherence became more clear. Elastic diffraction can only be observed if the surface illuminated coherently by the beam is itself coherent *i.e.* perfectly periodic. In GIFAD, the surface coherence has to be on the order of a few 100 Å to produce clearly visible elastic diffraction peaks and this is rather demanding in terms of surface preparation. Fortunately, LiF can be easily cleaved with large terraces if specific color

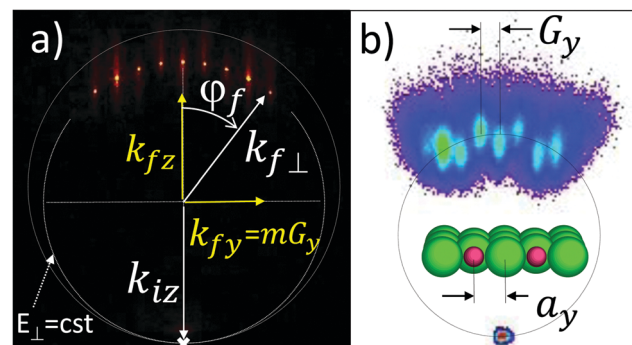


Fig. 4 (a) Diffraction pattern of 300 eV ⁴He on LiF along the <110> direction at $\theta_i = 1.08^\circ$ ($k_{\perp} = 14.3$ Å⁻¹). The white cross indicates the location of the beam before target insertion. The line between this cross and the specular spot indicates the scattering plane $k_{fy} = k_{iy}$. The elastic diffraction spots fall on the Laue circle of energy conservation: $k_{fy}^2 + k_{fz}^2 = k_{iz}^2$ and exhibit diffraction along the y direction only $k_{fy} = mG_y$. (b) Early diffraction image from ref. 55 where elastic diffraction was not visible.

centers are produced in the bulk by controlled exposure to neutrons or gamma rays.²⁸ Gentle annealing is enough to eliminate the color centers in UHV. Grazing incidence techniques, in general, are quite sensitive to the presence of defects. This sensitivity is heightened with non-penetrating techniques such as GIFAD because a single ad-atom or a molecule encountered along the comparatively long projectile trajectory is enough to perturb the scattering. The possibility of inducing thermal desorption of impurities is therefore important to observe diffraction.

3.2 Imaging detector

Several position-sensitive detectors are available²⁹ to detect helium atoms around 1 keV and all are based on micro-channel plates. For diffraction experiments and easy data analysis, the most important properties are good uniformity as well as an excellent integral and differential linearity (constant pixel size). A single, large-diameter micro-channel plate together with a phosphor screen and a scientific-grade camera demonstrated good results with a ≈ 70 mm active diameter on a 100 mm flange.³⁰

4 Brief theoretical aspects

So far, atomic elastic diffraction on a surface has been treated as the quantum dynamics of the projectile atom evolving in the potential energy landscape (PEL) often called PES for potential energy surface $V_{3D}(x,y,z)$ created by all surface atoms at equilibrium positions. In other words, quantum dynamics is the tool linking the unknown PEL to the measured diffracted intensities. Assuming that the quantum scattering can be treated exactly, both theoretical and experimental calculations are trying to measure the PEL as accurately as possible and to provide physical parameters such as atomic positions or the attractive physisorption depth.

4.1 Potential energy landscape (PEL)

Potential energy landscape is the potential energy $V_{3D}(\vec{r})$ of a target atom placed at a location \vec{r} of coordinates (x,y,z) above the surface. We define here two associated interaction potentials useful to understand the dynamics and describe GIFAD results. These are the mean axial $V_{2D}(y,z)$ and mean planar interaction potential $V_{1D}(z)$,

$$V_{2D}(y,z) = \int_{a_x} V_{3D}(\vec{r}) dx; \quad V_{1D}(z) = \int_S V_{3D}(\vec{r}) dxdy \quad (1)$$

where a_x is a periodic length along the low index x direction and S is a unit cell. Within the ASCA, GIFAD probes the $V_{2D}(y,z)$ interaction potential. Such an axial potential is represented in Fig. 2b where the large circles labeled F and Li correspond to the rows of fluorine and lithium atoms. In principle, several low index directions should be probed to better describe the full 3D PEL without ambiguity. The mean planar form, $V_{1D}(z)$, is useful to describe the general properties such as the mean trajectory length L or the mean interaction time τ , as well as the mean attractive well depth D .

4.2 PEL development over effective binary potentials

Describing the PEL over the full 3D volume above a unit cell is quite demanding. A useful data reduction procedure consists of adjusting the effective binary interaction potential attached to the surface atoms so that their summed contributions reproduce the calculated or inferred PEL: $V_{3D}(x,y,z) = \sum_{i,j,k} V_k(r_{ijk})$ where k

is an index for each surface atom in the lattice unit and i,j are the lattice indexes. With this approach, a reduced set of k binary interaction potentials is needed together with the equilibrium positions x_k, y_k, z_k of the k atoms of the surface lattice cell. For LiF, these are the locations of the lithium and fluorine ions as well as the few parameters describing the associated attractive and repulsive forces. This compact description is well suited to consider thermal displacements or fitting procedures between theoretical and experimental studies.

4.3 Quantum scattering models

The quantum dynamics of a helium atom having keV or tens of meV energies is not fundamentally different. However, since the wavelength is a hundred times smaller, the typical unit volume needed to describe an oscillation of the wave-function should be typically 10^6 times smaller. The time step also should be adapted to smaller values. Using the ASCA, only the slow motion in the (y,z) plane has to be considered and wave packet propagation^{11,31–33} or close coupling approaches^{34,35} have been successfully applied. The accuracy of the axial channeling approximation was investigated in detail by extensive 3D calculations compared with the simplified 2D ASCA.^{19,36,37} All methods developed for TEAS such as Bohmian trajectories^{38,39} or multi channel quantum defect theory^{37,40} should also apply to GIFAD within the ASCA. The close-coupling approach has shown to be particularly efficient³⁶ even in a situation where almost hundred diffraction channels are open.³⁴ We consider

here that quantum scattering can be solved and that a given PEL can therefore be compared with diffraction images.

4.4 Simplified scattering models

It is often desirable to have approximate methods allowing a qualitative understanding of the measured diffraction images. In this context, classical, semi-classical, and optical methods have provided valuable results. H. Winter and A. Schüller^{22,41} as well as M. S. Gravielle and J. E. Miraglia^{42,43} have developed a semi-classical approach. Using an eikonal approximation of small-angle scattering, they could treat the entire 3D scattering problem and verify the accuracy of the ASCA with classical trajectories, as pioneered by Danailov and Karpuzov.⁴⁴ M. S. Gravielle and J. E. Miraglia have also eliminated the so-called “rainbow divergence” appearing at the maximum lateral deflection angle⁴⁵ and demonstrated the sensitivity of the approach to the potential energy landscape.⁴⁶ The simplest approach is however the hard corrugated wall model (HCW) (see *e.g.* ref. 47). Assuming that the repulsive wall is quite abrupt, for instance, exponential, most of the deflection takes place in the vicinity of the turning point of the classical trajectory as illustrated in Fig. 2b. The HCW model considers a point-like specular deflection at the iso-energy potential surface $\tilde{z}(y)$ defined by $V(y,\tilde{z}(y)) = E_\perp$ and straight-line trajectories otherwise, for both the way in and out. The $\tilde{z}(y)$ surface acts as a corrugated mirror for the equivalent optical problem. This $\tilde{z}(y)$ function is also called the corrugation function and the difference between its maximum and minimum values is the full corrugation amplitude z_c . Within the HCW model, the probabilities of the diffraction into the j -th diffraction channel are calculated from ref. 47–50

$$P_j = \frac{k_{fz}}{k_{iz}} \left| \frac{1}{a_y} \int_0^{a_y} e^{-ijG_y y - i(k_{fz} + k_{iz})\tilde{z}(y)} dy \right|^2. \quad (2)$$

The HCW model has been mainly used to link diffracted intensity to a particular corrugation function $\tilde{z}(y)$. The HCW is not fully quantitative but it is enough to track simple tendencies, for instance, z_c decreases with energy relative to the LiF $\langle 110 \rangle$ direction while it increases along $\langle 100 \rangle$ ⁵¹ or to identify the charge transfer between Zn and Se atoms at the ZnSe surface.⁵²

5 Experimental elastic and inelastic diffraction

Both Fig. 1 and 4 display tiny spots visible on the diffraction images together with longer vertical stripes extending mainly along the polar exit angle θ_f (z direction). We assume here that these spots correspond to elastic diffraction where no energy is exchanged with the surface while the inelastic component is attributed to the excitation of phonons because the large band-gap efficiently prevents electronic excitation in the range of energy and incidence angle. These electronic excitations correspond to comparatively violent collisions populating the excitonic states and to electron emission.⁵³ Both were found to destroy the diffraction pattern.⁵⁴

Just like any other diffraction technique, the elastic diffraction intensity reveals the periodic component of the system investigated while the inelastic one contains information on the momentum transfer associated with the processes leading to energy exchange. In other words, the elastic diffraction indicates the location of the equilibrium positions, *i.e.* that of the center of the atomic wave function, while the inelastic component will be sensitive to the vibrational movement of these surface atoms as probed by the projectile atom.

Compared with photons or electrons, atoms have a large mass so that the recoil momentum transferred classically to the target atoms cannot be neglected. For an isolated target atom interacting with the helium projectile, momentum conservation implies that any projectile deflection is associated with the opposite recoil momentum of the target atom. In a solid or on a surface, the target atoms are not free to move but strongly coupled to their neighbors. This situation can be described by a Debye or Einstein model with each atom represented by a harmonic oscillator where a momentum change by δk may or may not lead to vibrational excitation. The oscillator is usually described by its quantized excitation energy $\hbar\omega_D \equiv k_B T_D$ where ω_D is the Debye frequency, k_B is the Boltzmann constant and T_D is the Debye temperature. For an atom in the vibrational ground state ($T \ll T_D$), this probability is

$$p_e = e^{-E_f/\hbar\omega_D} \quad (3)$$

known as the Mössbauer–Lamb–Dicke probability or probability for recoil-less emission in photon spectroscopy. This defines the Lamb–Dicke regime needed to cool down atoms down to nano kelvin in optical lattices. Here, two different classical points of views can be adopted.

One approach is to say that target atoms are displaced along z by σ_z , inducing a path difference of $2\sigma_z$ and a phase difference $2\vec{dk} \cdot \vec{\delta r} \approx 2dk_z \sigma_z$, with $d\vec{k} = (\vec{k}_f - \vec{k}_i)$. The intensity scattered at Bragg angle will be affected by an amount $e^{-(2d\vec{k} \cdot \vec{\delta r})^2}$ leading to the well known Debye–Waller factor. For a surface temperature T , the thermal distribution of z is Gaussian,

$$\sigma_z^2 = \langle z^2 \rangle = \frac{3\hbar}{2m\omega} \coth\left(\frac{T_D}{2T}\right) = \frac{3\hbar^2}{2mk_B T_D} \coth\left(\frac{T_D}{2T}\right). \quad (4)$$

To account for the absence of neighbor atoms in the region $z > 0$, a surface Debye temperature $T_{Ds} = T_D/\sqrt{2}$ is usually introduced.^{21,56}

The other approach considers the momentum $d\vec{k}$ transferred to a surface atom and evaluates, quantum mechanically, the probability that this transfer can induce vibration excitation. Classically, these separate views would be considered as different contributions but in quantum mechanics, momentum or spatial approaches are simply different ways to evaluate the same probability. To sum up, we simply say that the elastically diffracted intensity reveals the equilibrium position of the surface target atoms, just as any elastic diffraction technique.

Extracting elastic and inelastic contributions of the scattered intensity requires some care (see the discussion on inelastic diffraction in Section 7). For example, it was shown^{57,58} that

using the location of the direct beam (k_{iy}, k_{iz}) measured before target insertion as a reference point is crucial to define properly the scattering angle from the point of view of atomic collision (see Section 7).

The transformation of the raw diffraction pattern is as follows: first, the detector coordinates are slightly rotated so that the specular plane representing the z axis is perfectly vertical. Then, for any coordinates (k_{fy}, k_{fz}) on the detector one calculates the value of k_{\perp} as the radius of the circle passing by itself and by the direct beam with a center located on the $k_{iy} = 0$ vertical line. On the Laue circle of energy conservation, k_{\perp} is both the initial and the final value: $k_{\perp}^2 = k_{iy}^2 + k_{iz}^2 = k_{fy}^2 + k_{fz}^2$, while outside the Laue circle, it corresponds to $(k_{i\perp} + k_{f\perp})/2$.

To illustrate the transformation, we first consider the ideal situation displayed in Fig. 4a where the beam is well-aligned with the low index direction $k_{iy} = 0$ (or $\phi_i = 0^\circ$) so that the energy of the motion in the perpendicular plane is simply $E_{\perp} = E \sin^2 \theta_i$. Fig. 5a reports the same data after the transformation where the elastic diffraction spots are aligned horizontally. When projected onto the vertical direction corresponding now to k_{\perp} , the polar scattering profile allows an easy determination of the relative, elastic, and inelastic intensities. The polar distribution is fitted by two components, a narrow Gaussian with $\sigma = 6.7$ mdeg and a broader log-normal profile (eqn (5)) with a standard deviation twenty times larger $\sigma = 130$ mdeg corresponding to a log-normal dimensionless relative width $\sigma_{\theta_s}/\theta_s$ of 0.06 where θ_s is the full specular scattering angle $\theta_i + \theta_f$.

$$\text{LN}[\theta_s; w](\theta) = \frac{A}{w\theta\sqrt{2\pi}} \exp\left(\frac{-(\ln \theta/\theta_s)^2}{2w^2}\right) \quad (5)$$

For reasonably narrow distributions the relative width parameter w is close to the standard deviation divided by the median value $w = \sigma_0/\theta_s$. The intensity of the Gaussian

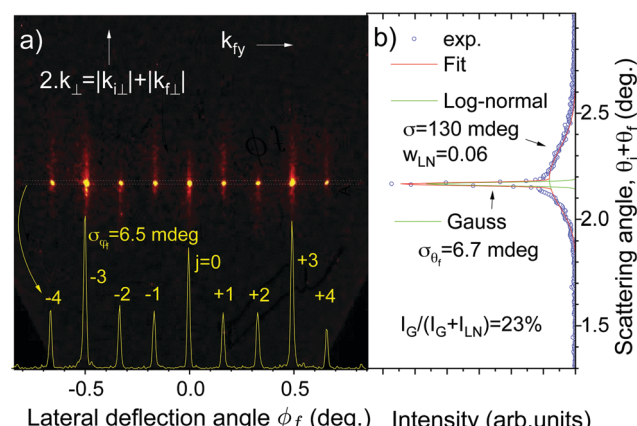


Fig. 5 Same as Fig. 4a but the vertical axis is now $k_{\perp\text{eff}} = |k_{i\perp}| + |k_{f\perp}|$ corresponding to the diameter of the dotted circle going through the beam in Fig. 4a. The Laue circle is now a horizontal line and the intensity on a 6 mdeg wide horizontal band is reported in yellow at the bottom. (b) Polar scattering distribution $P(\theta_f)$ obtained from vertical projection of (a) indicating two components, a narrow quasi-Gaussian and a much broader one having a quasi log-normal profile.

component represents 23% of all the intensity and should correspond to the absolute Debye–Waller probability. We use the width of the Gaussian distribution to define the size of the narrow band isolating the elastic profile displayed in yellow at the bottom of Fig. 5a. The profile can be analyzed using standard software to extract the diffraction intensities. A fit imposing equal line shape and equal spacing of the peaks provides a good accuracy on the measured intensities and line shapes. In the present case, the fit gives a quasi Gaussian line-width with $\sigma = 6.5$ mdeg comparable to the size of the primary beam *i.e.* to the angular resolution convoluted by the spatial resolution of the detector. This indicates that the elastic spot size is not limited by the surface coherence length.

6 Elastic diffraction

Fig. 5b shows that even at the specular angle, a significant fraction of the intensity can be present. In this example corresponding to $E_{\perp} = 106$ meV, the inelastic intensity corresponds to 77% of all the scattered intensity but only around 20% of the intensity on the Laue circle. *Stricto sensu* one should subtract this underlying 20% inelastic intensity and this can be achieved with well-tuned doubly differential filters such as the ‘‘Mexican hat’’.⁵⁸ However, in the regime where both elastic and inelastic diffractions are observed, their intensity distributions on the Laue circle were found to be equal.²¹ A tentative explanation of this observation is given in Section 7 describing our inelastic scattering model. In the present section, for simplicity, we will not discuss inelastic diffraction and we consider that the diffracted intensities correspond to the elastic component. We now examine the different types of measurements obtained by varying the beam parameters, their interpretation being postponed to the next chapters allowing qualitative comparisons.

6.1 Polar angle scan (θ -scan)

A polar scan is a step-wise variation of the angle of incidence θ_i at fixed energy and azimuthal angle ϕ_i . For simplicity, we consider here that this azimuthal angle ϕ_i is zero so that the projection of the beam direction on the surface coincides with a low axis direction of the crystal as in Fig. 4. Since $\theta_i \ll 1^\circ$, the Bragg angle $\phi_B = \arctan(G_y/k \cos \theta_i)$ is constant with a few 10^{-4} relative variation. A visual and compact way to display the evolution of the diffracted intensities in this polar θ -scan is to plot the intensities on the Laue circle in a 2D color map (diffraction chart). Since the diameter of the Laue circle is here proportional to the angle of incidence, the length of the half-circle above the surface grows linearly with the incidence angle producing an overall V shape. In Fig. 6, the white line indicates the maximum value of the lateral deflection expressed in diffraction order. This corresponds to a projectile atom scattered parallel to the surface, with $\phi_f = \theta_i$, and therefore $\theta_f = 0^\circ$, *i.e.* with all its momentum k_{iz} converted in the in-plane movement along the y direction. Like many diffraction charts, the one plotted in Fig. 6 is highly redundant, but this is also a

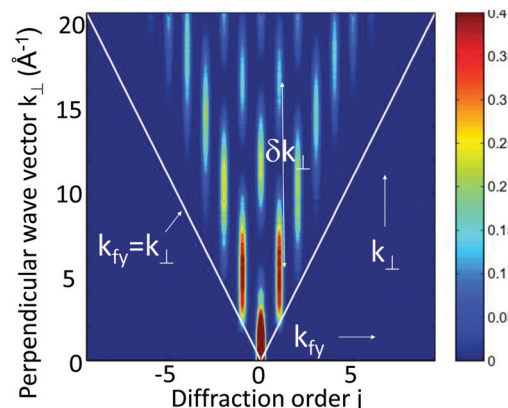


Fig. 6 Diffraction chart corresponding to a θ -scan recorded with 300 eV ^4He along the $\langle 110 \rangle$ direction. The Bragg angle is fixed and the angle of incidence θ_i determines the value of k_{\perp} . Here, 20 \AA^{-1} corresponds to $E_{\perp} = 208$ meV while the lowest values correspond to 2 meV.

warrant of high reliability. This can be qualitatively understood from the hard corrugated wall model. Within the HCW, each horizontal line in Fig. 6 corresponds to one iso-energy corrugation function and since the shape of these curves evolves only slowly (see *e.g.* Fig. 15b), changing the value of E_{\perp} can be viewed as illuminating a given grating with different values of λ_{\perp} . The most simple case would correspond to a cosine corrugation function $\tilde{z}(y) = z_c/2 \cos(2\pi y/a_y)$ where z_c is the full corrugation amplitude and a_y is the lattice parameter associated with the periodic row structure of the axial potential $V_{2d}(y, z)$. In this case, eqn (2) indicates that the diffracted intensities are given by $I_j = J_j^2(2\pi z_c/\lambda_{\perp})$ where J_j is the Bessel function of rank j . The advantage of this corrugation function is that the whole diffraction chart can be modeled with only one parameter z_c . Each diffraction order relative intensity I_j can be seen as an independent measurement of the path difference of the two trajectories leading to a lateral deflection by $j \times \phi_B$.

When recorded on a sufficiently broad angular range, the inelastic diffraction prevails at a large incidence angle and the diffraction chart nicely shows the progressive broadening of the diffraction peaks with the energy E_{\perp} .²² However, both elastic and inelastic diffractions contribute to the Laue circle so that the measured width is ambiguous. For instance, in Fig. 5, the lateral deflection distribution displays narrow elastic diffraction peaks while the energy dependent inelastic contribution may dominate under different conditions. When the elastic component dominates, as in Fig. 4a and Fig. 6 the peak width appears constant while it does slowly increase in Fig. 7 and in ref. 22 where elastic diffraction is not clearly visible.

6.2 Energy scan (E -scan)

An energy scan is a step-wise variation of the primary beam energy E while maintaining the angles of incidence θ_i and azimuthal ϕ_i fixed. During an E -scan, the radius of the Laue circle is constant but the Bragg angle $\phi_B = \arctan(G_y/k \cos \theta_i)$ gets lower as the energy increases so that more diffraction orders can be observed until they cannot be resolved

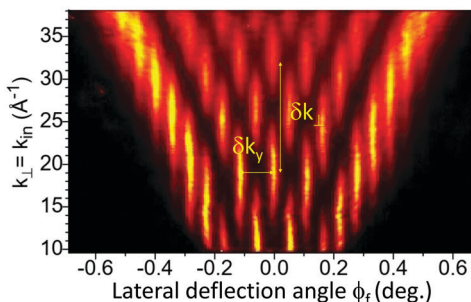


Fig. 7 Diffraction charts of 500 eV neon on LiF $\langle 110 \rangle$ recorded at incidence angles θ_i between 0.25 and 1° corresponding to $E_\perp = 9.5$ and 76 meV, respectively. In the paraxial region, a pseudo period is observed, $\delta k_\perp \sim 13.3 \text{ \AA}^{-1}$ and $\delta k_y \sim 2G_y$.

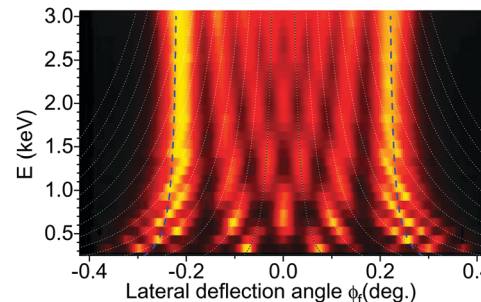


Fig. 8 Diffraction charts for neon impinging on LiF $\langle 110 \rangle$ recorded at fixed incidence of 0.42° and at incident energies between 300 eV and 3 keV.

experimentally. Fig. 8 displays an E -scan of neon atoms on a LiF surface along the $\langle 110 \rangle$ direction with $\theta_i = 0.42^\circ$ and $\phi_i = 0^\circ$. The locations of the Bragg peaks are indicated by dotted white lines.

One interesting aspect of the E -scan is that the area illuminated on the crystal surface remains constant, allowing more reliable identification of small variation of the diffracted intensities. On a microscopic level, the length of the trajectory is also expected to remain constant as long as attractive forces can be neglected which offers an interesting opportunity for the investigation of inelastic processes. The number of binary collisions should remain constant as well as the associated deflection angle.

6.3 λ diffraction chart

Another presentation of the diffraction data was proposed by Winter and Schueler.²² It consists of a diffraction chart plotted as a function of the projectile wavelength λ_\perp irrespective of the way the data have been collected. This would be interesting mainly for data collected in the elastic regime because the ASCA tells us that the only relevant parameters are the ones associated with the motion in the plane perpendicular to the low index direction. This can be the energy E_\perp , the wave-number k_\perp or the wavelength λ_\perp . However, diffraction charts also display the measured width of the diffraction peaks and this was shown to be associated mainly with the limited surface coherence and/or with inelastic processes which depend also on the actual projectile energy (see Section 7). In practice, λ diffraction charts offer an easy presentation of the nodal structures (see Fig. 15a).

All diffraction charts presented provide a clear 2D picture with their own advantages. These can illustrate specific features such as a slow variation of the corrugation amplitude seen as a variation of the oscillation rate of the specular intensity with k_\perp or a variation of the rainbow deflection angle at high or low velocity. Perhaps the most important prediction of the ASCA is that the elastic diffracted intensities should depend only on the energy E_\perp irrespective of the values of E and incidence angle θ_i . Fig. 22 shows that indeed the red circles and blue triangles corresponding to the θ -scan and the E -scan in Fig. 7 and 8 respectively fall on top of each other.

6.4 Azimuthal scan (ϕ -scan)

Fig. 9 displays a typical diffraction image recorded when the azimuthal direction does not coincide with a low axis direction of the crystal. It corresponds to ^4He atoms with 460 eV energy, an incidence angle $\theta_i = 0.9^\circ$ and an azimuthal angle $\phi_i = 0.45^\circ$. The elastic diffraction spots are still aligned on a circle passing by the primary beam position and the specular spot. The main difference resides in the center of the Laue circle now shifted by 0.45° corresponding to the intercept with the low index direction. The projection of the scattering plane on the detector, defined by the line connecting the specular spot to the direct beam location, is not the diameter of the Laue circle anymore, which is now $2k_\perp = 2\sqrt{k_{iy}^2 + k_{iz}^2}$. This radius k_\perp corresponds to the magnitude of the wavevector in the (y,z) plane. In this plane, the vector \vec{k}_\perp corresponds to a particle trajectory no longer perpendicular to the surface but impacting the atomic rows of the $V_{2D}(y,z)$ potential with an angle of incidence

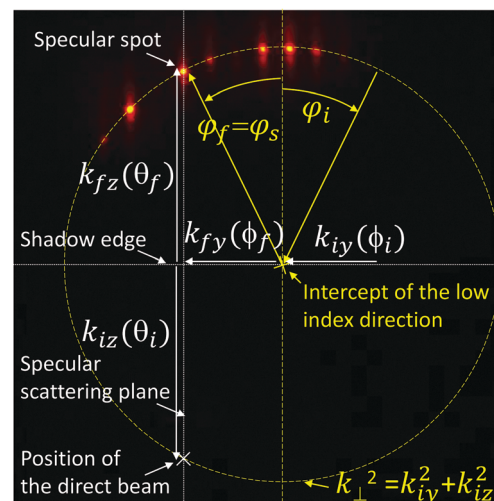


Fig. 9 Diffraction pattern of 460 eV ^4He impinging along LiF $\langle 110 \rangle$ with $\theta_i = 0.9^\circ$ and an azimuthal incidence angle $\phi_i = 0.45^\circ$. The white dotted lines correspond to the intercept with macroscopic planes; the horizontal shadow edge of the surface plane and its perpendicular specular scattering plane which contains both the incident and specularly reflected projectiles. It corresponds to the impact of an effective particle with a momentum $\hbar k_\perp = \hbar\sqrt{k_{iy}^2 + k_{iz}^2}$ with an incidence angle $\phi_i = \arctan(k_{iy}/k_{iz}) \approx 26^\circ$ with respect to the surface normal.

$\varphi_i = \arctan(k_{iy}/k_{iz}) \approx \arctan(\phi_i/\theta_i)$. This experimental evidence of ASCA is similar to the one presented in ref. 59 for inelastic diffraction. However, the definition of the Laue circle is completely unambiguous only in the elastic regime.

The azimuthal scan corresponds to a variation of the azimuthal angle ϕ_i (see Fig. 10 for the definition of the scattered angles). During an azimuthal scan several low index directions can be identified providing the basis of atomic triangulation measurements^{60,61} detailed in the next section. We focus here on the behavior of the diffraction pattern close to a given low index direction. As detailed above, according to the ASCA, an azimuthal scan corresponds to a variation of the incidence angle ϕ_i in the (y,z) plane. This was first investigated by Seifert *et al.*⁵⁹ and it is illustrated in Fig. 11 where the successive Laue circles of elastic diffraction indicate the progressive evolution to grazing scattering angles in the (y,z) plane. It also shows that the effective energy associated with the motion in the (y,z) plane, here represented by yellow arrows linking the center of the Laue circle to the specular spot, increases with the azimuthal angle ϕ_i .^{20,59}

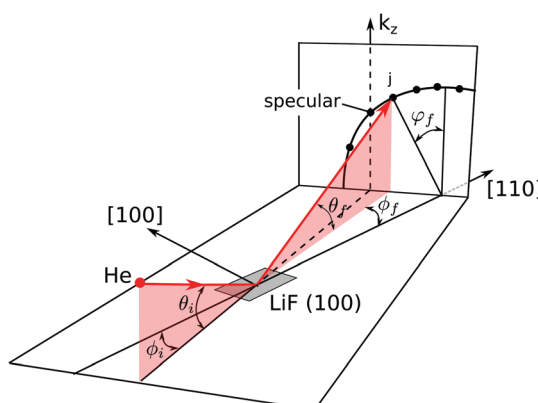


Fig. 10 Scattering geometry under misalignment. An helium atom impinges on a LiF surface with a polar incidence angle θ_i and azimuthal (misalignment) incidence angle ϕ_i with respect to the $[110]$ direction of the surface. A diffraction order j is located by the lateral deflection angle ϕ_f , the polar exit angle θ_f and the deflection angle φ_f , the scattering plane in red, corresponds to $j = 1$. During a ϕ -scan, the position of the specular spot on the detector remains fixed.

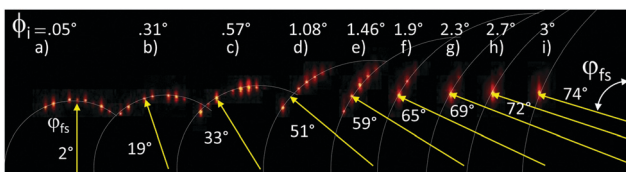


Fig. 11 Juxtaposition of nine diffraction patterns of 460 eV ${}^4\text{He}$ corresponding to an incidence azimuthal angle ϕ_i of 0.05, 0.3, 0.57, 1.1, 1.9, 2.3, 2.7 and 3° relative to the $\langle 110 \rangle$ direction. This ϕ scan is also a k_{iy} scan and corresponds to a variation of the effective angle of incidence $\varphi_i = \arctan(k_{iy}/k_{iz})$, but is associated with an increase of the effective energy E_\perp due to the increase of k_\perp illustrated by the Laue circle. The yellow arrows indicate the specular spot with $k_{fz} = -k_{iz}$, $k_{fy} = k_{iy}$. During the experiment, the location of the specular spot on the detector stays fixed.

When the incidence angle φ_i in the perpendicular plane becomes itself grazing, the diffracted intensities gradually reduce to a single specular peak. In this (double) grazing regime, the softness of the potential cannot be neglected anymore because it is responsible for the smooth deflection of the projectile leading to fully specular reflection.⁵⁹ This is quantitatively estimated by the obliquity factor calculated by Henkel *et al.*^{23,62} and should provide an asymptotic behavior for the tails of the triangulation peaks in Fig. 13. This is the GIFAD equivalent of the situation where a pronounced reduction of the in-plane diffraction was observed by Fariñas *et al.*²⁴ in TEAS when the angle of incidence with the surface plane reached $\approx 20^\circ$. This situation has been well reproduced both by quantum scattering calculations²⁰ and by semi classical trajectory calculations.⁵⁹ Ruiz *et al.* also proposed a description in terms of quasi-resonance that should apply to most GIFAD situations.⁶³ Due to the very small Bragg angles in GIFAD, it can be difficult to reach the perfectly aligned condition $\phi_i \ll \phi_B$. From the experimental point of view, it is important to estimate first-order corrections to better compare images recorded with small azimuthal angle $\phi_i \simeq \phi_B$. The HCW formula in eqn (2) is only valid for $k_{iy} \ll G_y$, and simple 1st order perturbation theory by Henkel *et al.*²³ does not fulfill time reversal symmetry. This was empirically corrected by Debiossac *et al.*⁶² as illustrated in Fig. 12c. A second-order perturbation theory has been recently proposed by Pollak and Miret-Artés⁶⁴ that should allow even better corrections. During an azimuthal scan, the angle of incidence θ_i should remain fixed. Therefore the direction normal to the surface should coincide with the azimuthal rotation axis with a high accuracy which is particularly demanding in a bakeable UHV system compatible with transfer systems. In practice, recording the specular spot location during a complete 360° azimuthal scan allows a precise measurement of the residual tilt angle ϑ in the form of a cosine oscillation $\theta_s \simeq \theta_0 + \vartheta \cos \phi - \phi_0$ with a defect ϑ usually of a few tenths of a degree. Measuring the azimuth ϕ_0 for which the observed specular scattering is maximum allows an easy

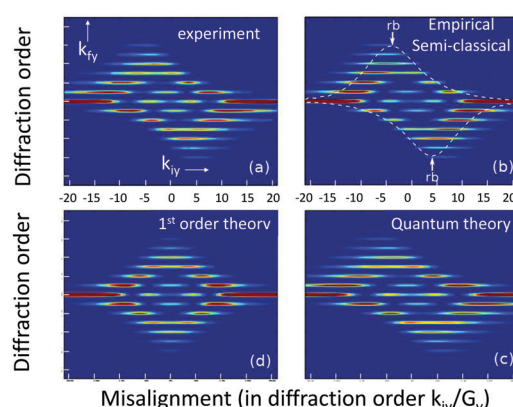


Fig. 12 (a) Evolution of the diffracted intensities of 460 eV ${}^4\text{He}$ impinging at $\theta_i = 0.93^\circ$ reported versus the azimuthal misalignment angle ϕ_i relative to the $\langle 110 \rangle$ direction expressed in diffraction order $G_y = 2.2 \text{ \AA}^{-1}$, $\phi_B = 0.133^\circ$. (b-d) are for calculations from ref. 20, 23 and 62, respectively.

correction by adjusting a cosine compensation of the polar angle during an azimuthal scan to provide a stable incidence angle θ_i during rotation.⁶⁵ Note that the presence of a sharp elastic diffraction spot is also very convenient to identify the presence of various surface mosaicity that can arise from thermal or mechanical shock.⁶⁶

6.4.1 ϕ -scan and atomic triangulation. The azimuthal scan is usually the first experiment performed after the insertion of a new sample in the UHV chamber. This allows precise measurement of the main crystallographic directions difficult to track precisely in a transfer system. Most often, diffraction is not observed immediately because of molecular adsorption or any other reason such as limited coherence. We present here triangulation measurements offering a natural extension of the diffraction data into the classical limit where diffraction does not exist. The word triangulation was introduced by Pfandzelter *et al.*⁶⁷ to designate an azimuthal scan during which the secondary electron emission following the impact of 25 keV H⁺ ions at grazing incidence was recorded. Maxima in the electron yield were assigned to low index directions of the topmost layer because, with $E_{\perp} \approx 30$ eV, the trajectories deep inside the valleys are significantly longer. By following the new direction appearing after exposure to metallic vapor, they could identify crystallographic properties of freshly grown over-layers. With atoms having an energy E_{\perp} below one eV, electron emission is not present and another contrast mechanism has been proposed, compatible with a GIFAD apparatus equipped with a position-sensitive detector. Feiten *et al.*⁶⁰ monitored the maximum intensity during the azimuthal scan observing dips associated with the low index directions while Kalashnyk *et al.*⁶¹ directly tracked the width and mean position of the scattering profile. Peaks of maximum width associated with low index directions together with a characteristic swing of the mean scattering plane were reported. Both observations were recorded under conditions where diffraction was not or hardly visible. In the following we show similar measurements performed with 460 eV helium.²⁰

Fig. 13 shows the evolution of the mean scattering width $\Delta\phi_f$ evaluated automatically from the diffraction image as the standard deviation σ_{ϕ_f} times 2.35, a number that would coincide with the full width at half maximum (fwhm) for a Gaussian distribution. We use the scattering width $\Delta\phi_f$ divided by the angle of incidence θ_i as a number that does not depend rapidly on the angle of incidence θ_i . Both low index directions $\langle 110 \rangle$ and $\langle 100 \rangle$ appear with a very large contrast and their evaluation could be compared with quantum or classical calculation on a quantitative basis. The data around $\phi_i = 0^\circ$ correspond to the values plotted in Fig. 12. Here again, the width is strongly related to the rainbow scattering angle $\Delta\phi_f \sim 2\phi_r$ but it is defined without ambiguity through the variance of the measured scattering intensities. Such evaluation remains meaningful even when only a limited number of diffraction orders is observed, as in Fig. 4a making the rainbow angle impossible to measure accurately. The position, amplitude, and width of these triangulation peaks are not expected to change significantly with the beam energy or with the surface quality.

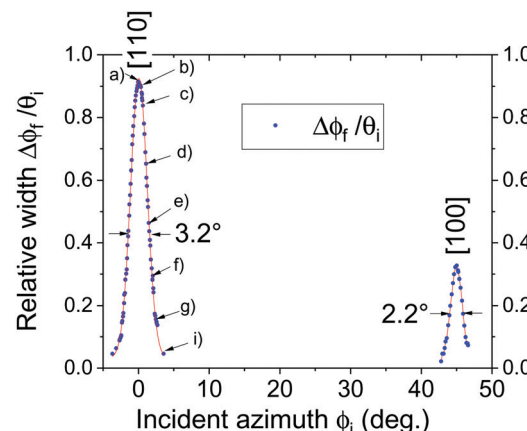


Fig. 13 For 460 eV ^4He on a LiF (001) surface,²⁰ the azimuthal scattering width $\Delta\phi_f$ (fwhm) divided by the incidence angle θ_i is reported as a function of the incidence azimuthal angle ϕ_i revealing the low index directions $\langle 110 \rangle$ and $\langle 100 \rangle$. The images in Fig. 11 corresponds to the locations indicated on the left peak. $\Delta\phi_f$ is the width along k_y divided by the radius of the Laue circle. Both the amplitude and width of these triangulation peaks are expected to be hardly modified whether diffraction is observed or not.

Only the base level is expected to rise rapidly from a value close to the width of the primary beam when diffraction conditions are good as in Fig. 11 up to much larger values when the surface has a limited coherence length and/or is partly covered by adsorbates.

In addition to the increased scattering width when the azimuthal angle ϕ_i approaches a low index direction, a guiding effect was demonstrated.²⁰ Using the same data, Fig. 14 shows three different representations of the mean vertical and lateral deflection taking place during an azimuthal scan when passing through a low index direction. The oscillation of the mean lateral deflection $\langle \phi_f \rangle$ was observed even without diffraction in ref. 61. However, in the inelastic regime, the weaker vertical

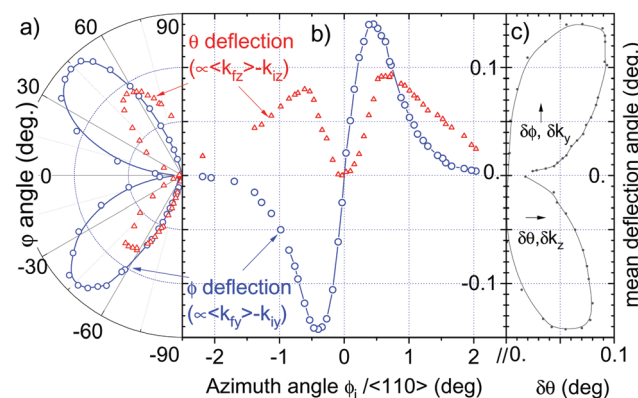


Fig. 14 For 460 eV ^4He on a LiF (001) surface at an incidence polar angle $\theta_i = 0.48^\circ$ and variable azimuthal incidence angle ϕ_i , the mean lateral angle $\langle \phi_f \rangle$ and the mean azimuthal exit angle $\langle \theta_f \rangle$ referred to the specular beam are reported in three different forms. (b) Cartesian plot versus the azimuthal angle ϕ_i referred to the $\langle 110 \rangle$ direction.²⁰ (a) Polar plot as a function of the angle $\phi_i = \arctan(k_{iy}/k_{iz})$. (c) Trajectory of the mean impact position ($\langle \theta_f \rangle$, $\langle \phi_f \rangle$) as the incident azimuthal angle ϕ_i is varied.

deflection (along θ_f) is easily blurred by the broad log-normal inelastic polar scattering profile.

6.5 High perpendicular energies, the topology

For large values of E_\perp of the motion in the perpendicular plane, the associated wavelength becomes comparatively small allowing a good spatial accuracy. This is true in microscopy and applies also to diffraction. Let us assume that the HCW model is exact and that one tries to measure the shape of the corrugation function $\tilde{z}(y)$ over the projected lattice cell a_y , for a given value of E_\perp . Due to the interferometric nature of diffraction, a resolution between $\lambda/10$ and $\lambda/100$ can be expected in the z direction depending on the accuracy in measuring the diffracted intensities. Along the y direction, the accuracy should scale with λ_\perp meaning that the shape $\tilde{z}(y)$ along y may have n significant points where n is the number of observed diffraction peaks. In addition, at large values of E_\perp the exact contribution of attractive forces, which are still difficult to evaluate qualitatively, are reduced allowing more confidence in the evaluation of the PEL. For LiF the projected lattice parameter a_y along the $\langle 110 \rangle$ and $\langle 100 \rangle$ directions is 2.01 Å and 2.85 Å respectively while a ${}^4\text{He}$ atom with 100 meV and 1 eV energy has a wavelength of 0.45 Å and 0.14 Å, respectively. The obvious limitation being that the diffraction peaks should be well-resolved to allow a good measurement of their intensities.

The first quantitative attempt to go beyond simple corrugation measurements and to use GIFAD data for topology was proposed by Schueller *et al.*³² using *ab initio* DFT calculations and a wave packet propagation technique. Compared with diffraction data in Fig. 15a, they proposed a rumpling of the lithium ions by 0.05 ± 0.04 Å below the fluorine plane as well as an overall PEL displayed in Fig. 15b. A striking result is that the shape of the corrugation function $\tilde{z}(y)$ associated with successive values of E_\perp appears very similar. This indicates that, in the optical limit and in this energy range, the diffraction data should correspond qualitatively to illuminating a grating of fixed shape $\tilde{z}(y)$ with a variable wavelength λ_\perp providing very high redundancy. In this case all the diffraction orders evolve smoothly and can be interpreted easily with optical models (see *e.g.* ref. 34 and 68). The central region of the diffraction chart where $\phi_f \sim 0^\circ$ corresponds to quasi specular reflection

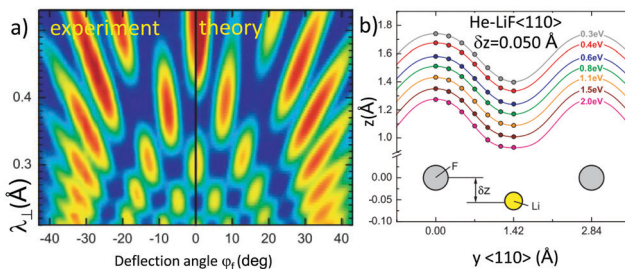


Fig. 15 (a) Comparison of experimental and calculated diffraction charts of He on LiF along $\langle 110 \rangle$ as a function of the wavelength λ_\perp . (b) Calculated potential energy landscape and, in the bottom the atomic positions highlighting the rumpling by 0.05 Å of the Li^+ ions. Image taken from ref. 32.

i.e. to trajectories bouncing on a flat section of the PEL either on top or in the bottom of the valleys. In this paraxial region the pseudo period $\delta k_\perp \sim 10.5 \pm 0.2 \text{ \AA}^{-1}$ observed in Fig. 6 for helium atoms and of $\delta k_\perp \sim 13.3 \pm 0.3 \text{ \AA}^{-1}$ in Fig. 7 for neon atoms can be interpreted as due to a full corrugation amplitude $z_c = \pi/\delta k_\perp \sim 0.3 \text{ \AA}$ and 0.24 Å when probed by helium and neon, respectively, without any further assumption on the exact shape. The lower corrugation probed by neon could be due to the larger size of the $2p^6$ outer shell increasing the repulsive force by a factor ~ 3 compared with the two electrons of the $\text{He}(1s^2)$ so that the neon atom is repelled slightly further away than helium atoms, where the corrugation is less. Along the y direction, the pseudo period of two diffraction orders between successive maxima in Fig. 6 indicates that the bottom sits in between the two top of the valleys. More complex shapes of the PEL could be measured³⁴ with this optical model and with a surprising accuracy regarding its simplicity, probably because measuring such pseudo periods eliminates quantum corrections needed to predict the absolute locations of the maxima.

The progression of the scattering profiles with higher values of E_\perp is reported in Fig. 16 using 5 keV ${}^4\text{He}$ projectiles. The inelastic diffraction dominates and clear diffraction peaks can be resolved up to ≈ 1.5 eV. The scattering profiles are progressively structured in groups adopting a radial nodal structure identified as the supernumerary rainbows⁶⁹ by analogy with the well known optical effect. These maxima (and minima) correspond here to successive phase match (and mismatch) between the two trajectories scattered at the same angle with the lattice cell. For the outermost rainbow, classical trajectories scattered at the maximum deflection angle originate from both sides of the inflection point of the corrugation function defined by $d^2\tilde{z}(y)/dy^2 = 0$ and can be chosen arbitrarily close to each other and are therefore always in quasi-phase match producing the genuine rainbow, ubiquitous in scattering theory.

As discussed above the path difference for the trajectories bouncing on top and bottom of the valley and contributing to

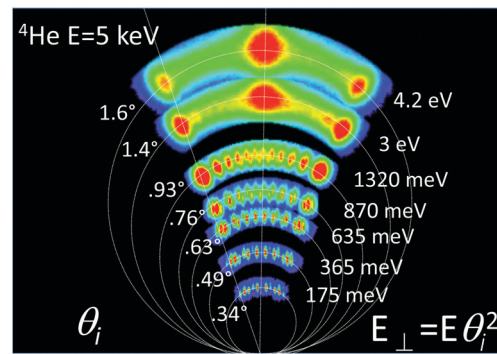


Fig. 16 Superposition of seven diffraction patterns measured with 5 keV ${}^4\text{He}$ projectiles on LiF aligned along the $\langle 110 \rangle$ direction. The angle of incidence θ_i is indicated on the left and the corresponding energy E_\perp on the right. All Bragg peaks can be resolved until $E_\perp = 1.5$ eV. Supernumerary rainbow structure (see text and Fig. 17) dominates above $E_\perp = 300$ meV. Above $E_\perp = 2$ eV only the supernumerary rainbow structure persists but slowly weakens. At 4.2 eV only broad intensity variation persists as detailed in Fig. 18.

specular region amounts to $2 \times z_c$ so that the phase difference is expected to increase progressively from zero at the outer rainbow φ_r to $2k_\perp \times z_c$ in the center $\phi_f = 0^\circ$ or $\varphi_f = 0^\circ$. A maximum of the diffracted intensity will be observed each time that the phase difference is close to a multiple of 2π . For a cosine corrugation function, the maxima would be those of the Bessel functions representing its Fourier transform. For a more complex shape of the corrugation function, the exact location of the maxima should allow accurate determination of the corrugation function.⁷⁰ The nodal structure tends to be more visible in the $\varphi = \arctan(\phi/\theta)$ coordinates because the inelastic diffraction images can be seen as a local θ -scan (see Section 7) where the nodal lines are tilted as clearly visible in Fig. 7 and 16. Fig. 17 displays a scattering profile recorded with a perpendicular energy $E_\perp = 1.45$ eV together with the intensity distribution corresponding to the radial projection where twelve maxima are observed with a minimum in the center. This tells us that the specular phase shift in the center should be around $5.5 \times 2\pi$ giving $z_c \approx 0.33$ Å, a fair estimate of the corrugation amplitude probed by a helium atom at this energy E_\perp . Independently, the location of the rainbow angle at $\varphi_r = 36^\circ$ indicates that the inflection point (where $d^2\tilde{z}(y)/dy^2 = 0$) in the corrugation function corresponds to an angle of $d\tilde{z}(y)/dy = \varphi_r/2 = 18^\circ$. Note that the inner maxima corresponding to the fifth supernumerary rainbow are in fact made of still resolved $j = \pm 1$ diffraction order while the dip in between corresponds to the quasi-extinct specular spot. This corresponds to the paraxial structure identified in the previous section where the intensity switches from maximum to minimum for adjacent diffraction orders.

At even higher values of E_\perp , Fig. 16 shows that the nodal structures also progressively disappear producing smooth scattering profiles. Similar profiles have been recorded at keV energies and were considered to be entirely classical however, most often, classical trajectory simulations were struggling to

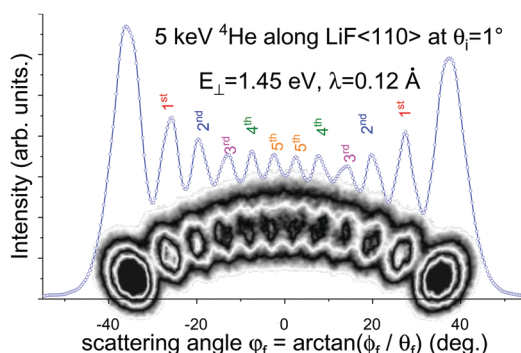


Fig. 17 Scattering profile of 5 keV ${}^4\text{He}$ atoms at $\theta_i = 1^\circ$ incidence on LiF $\langle 110 \rangle$ expressed as a function of angle φ_f in the perpendicular plane where the nodal structure is more visible. Along with the external rainbow peaks at $\varphi_r \approx 36^\circ$, five additional supernumerary rainbow peaks are observed indicating a full corrugation amplitude of $z_c = 0.33$ Å (see text). Close to the center, the inelastic Bragg peaks are still resolved showing a π shift from j to $j + 1$ while the four diffraction orders at the outer rainbow angle φ_r are almost in phase but are still resolved in the natural diffraction coordinates ϕ_f .

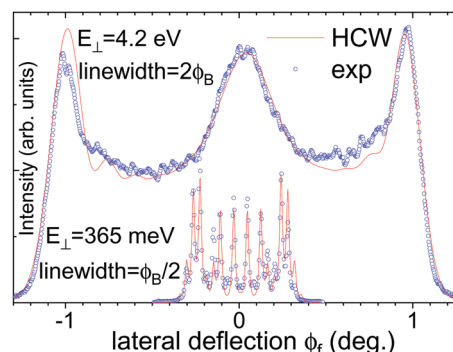


Fig. 18 Diffraction profiles for 5 keV ${}^4\text{He}$ along LiF $\langle 110 \rangle$ at $E_\perp = 4.2$ eV (top) and 365 meV (bottom) are fitted by the HCW formula of eqn (2). In both spectra, the Bragg angle is $\phi_B = 0.04^\circ$ but the individual width of the diffraction peaks was chosen as 0.02° for the bottom spectrum and 0.08° for the top one. In this latter case, the rapid oscillation taking place every second order in the paraxial region is indeed present but not visible; it is efficiently washed out.

reach a fair agreement. The unexpected surprise is that the optical HCW model provides a good description of the data in the whole range of E_\perp , solving directly the rainbow divergence and the fast quantum oscillation without explicitly addressing the coherence/decoherence issue. Fig. 18 displays the lateral deflection profile of the topmost pattern in Fig. 16 together with a fit using the HCW model with only two terms in the Fourier expansion of the corrugation function $\tilde{z}(y) = 0.15 \cos(2\pi y/a_y) + 0.026 \cos(4\pi y/a_y)$ in Å. The outermost rainbow angle is well reproduced as well as the central broad maximum. This latter can only be present if the corrugation function is not a pure cosine. Qualitatively, it corresponds to a flattening of the bottom of the valley due to the presence of Li^+ ions visible in Fig. 15b. Compared with the electrons of the $2\text{p}^6 \text{F}^-$ ions forming the valence band the density of the 1s^2 electrons of Li^+ ions is much more compact and decays more rapidly. For these reasons, the Li^+ contribution can be almost neglected at a large distance but Fig. 18 clearly illustrates their contribution at a closer distance to the surface.⁵¹ With KCl, the effect is much more pronounced, producing a drastic change in the diffraction chart when the K^+ ions produce a second maximum in the corrugation function.^{40,46,71} Fig. 18 also displays a comparable fit of the diffraction pattern recorded at lower angle of incidence θ_i i.e. having the same Bragg angle $\phi_B = 0.04^\circ$. The main difference is that the width of the individual inelastic peaks is half the Bragg angle for the bottom one and twice the Bragg angle for the top one. In both cases, the HCW is fully coherent and predicts rapid intensity oscillations, for instance in the paraxial region, but, on top, these are efficiently washed out simply by considering a line profile $2\phi_B$ broad. The strong attenuation of oscillation amplitude of the supernumerary rainbows is also surprisingly well reproduced, probably because their frequency also increases with E_\perp as illustrated by the variation between Fig. 17 and 18. The line-widths used here result from an adjustment to the data and are much larger than the width of the primary beam indicating a dominant contribution from the inelastic width discussed in Section 7

and not to spot size effects as discussed by Frisco and Gravielle.⁷² However, from the HCW point of view, these contributions could have a similar effect on the visibility of the fringes. It should also be stressed that the HCW was used here only to illustrate that the progressive decoherence can be modelled as a width, and the numerical values obtained with the HCW are only qualitative. Quantitative values, as obtained by quantum dynamics, are usually slightly different.

6.6 Low perpendicular energies, the attractive forces

At low values of E_{\perp} , the influence of the attractive forces, the van der Waals, and, for ionic crystals, the polarisation forces become important. Since these usually have a longer range than the repulsive one, a small physisorption well with depth D may be present. This physisorption depth plays a key role in the early stage of chemical reactions at surfaces although difficult to measure or to calculate accurately. TEAS is a reference technique⁷³ and in combination with high resolution spin-echo methods⁷⁴ allows for a precise determination of physisorption well through bound state resonance measurements. These resonances correspond to a sharp modification of the diffracted intensities and were first observed by Frisch and Stern⁷⁵ only a few years after de Broglie prediction that all particles should have an associated wavelength. Assuming, for simplicity, that the attractive forces are directed along the z direction perpendicular to the surface, a minimum energy $E_z > D$ is required to escape from the surface attraction. A particle arriving from the vacuum necessarily has a kinetic energy larger than D above the well, but after interactions with the surface the velocity component along z might not be enough to escape from the attractive well. Classically, it bounces back on the surface and encounters as many additional impacts as needed until the energy along z is again larger than D . Quantum mechanics is significantly different: the allowed deflection is limited to multiples of the reciprocal lattice vector G_y and the allowed bouncing trajectories should correspond to bound states of the potential well explaining the resonant behavior. More importantly, all different paths leading to a given diffraction order interfere, building a large amplitude resonance.

With GIFAD, only the three lowest resonance could be measured.³³ Fig. 19, corresponding to the diffraction chart in Fig. 6, shows that the measured amplitude of the resonance is significantly reduced compared to the 100% theoretical predictions by wave packet propagation technique.³³ This reduction was interpreted as due to the finite coherence length of the surface. The nature of the resonance on the average potential $V_{2D}(y,z)$ is similar to the one in TEAS and the time τ_b needed for a rebound is the same. However, compared with TEAS, the distance $x = v_x \tau_b$ spanned is longer by several orders of magnitude and any ad-atom or lack of periodicity will perturb the interference between direct and indirect scattering. The 0.5 meV width of the resonance may have different contributions but if associated with the coherence length the corresponding value would be 0.2 μm .

In conclusion, bound states resonances can also be measured with GIFAD but the large projectile velocity implies

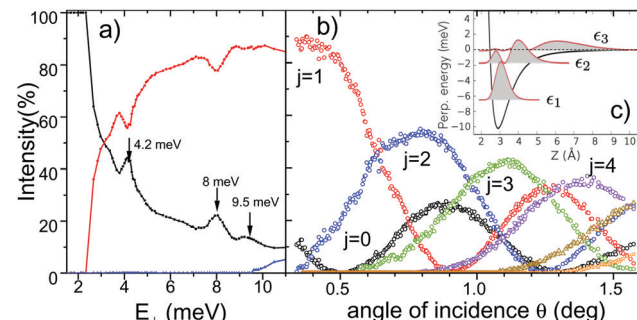


Fig. 19 For 300 eV ^4He on LiF along the $\langle 110 \rangle$ direction,³³ the intensity of the diffraction orders j (\pm added) is reported for E_{\perp} between 2 meV and 233 meV. (a) Corresponds to the lowest values of E_{\perp} displaying bound state resonances while a smooth evolution is observed above in panel (b). The inset is a schematic view of the mean interaction potential $V_{1D}(z)$ showing the bound states.

long distances between successive bumps so that a very long surface coherence is required. Even with several thousand Å coherence length, only weakened resonance could be observed and only when two diffraction orders interfere producing, in theory, a 100% amplitude in the intensity associated with the resonance.

With neon atoms, the number of diffraction orders is much larger and so is the number of bound states.⁷⁶ The diffracted intensities plotted in Fig. 22 combining the data of the two diffraction chart in Fig. 8 and Fig. 7 do not reveal their presence. However, in the E -scan plotted in Fig. 8, a clear increase of the maximum deflection angle ϕ_f is visible at the lowest values of E_{\perp} . The increase of the maximum deflection angle is often associated with an increase of the effective corrugation because for a simple shape of the corrugation potential the maximum slope is supposed to be proportional to the corrugation amplitude. Since lower values of E_{\perp} correspond to scattering taking place at a larger distance z to the surface plane, the corrugation is expected to decrease. This apparent contradiction was interpreted qualitatively as a refraction effect taking place on the way out. The projectile is accelerated toward the surface by an amount D so that the impact energy $E_{\perp} + D$ does not tend to zero revealing a quasi-constant distant of approach and a stable maximum deflection angle close to the rainbow angle φ_r . When leaving the repulsive region, the projectile enters the region where the attractive forces dominate and, assuming that these forces are directed towards the surface, the energy D has to be subtracted from the motion along z producing an increased deflection angle ϕ_f as illustrated in Fig. 20. This outlines the analogy with refraction in optics when light is emitted from a planar media with a refraction index larger than in the region of observation. The blue dashed line in Fig. 8 is obtained from a simple model using a value of $D = 10$ meV. A quantitative evaluation has been performed by a quantum diffraction code confirming the coarse estimation which will be described in the next section. We try here to extend this type of measurement to helium where the increased deflection is not easily visible at low energies because only two or three diffraction orders are

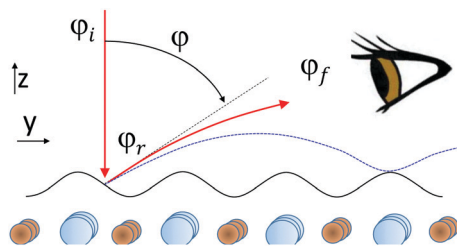


Fig. 20 Schematic view of the refraction effect. When the effective energy E_{\perp} is much larger than the well depth D , the deflection angle φ_f is close to the rainbow angle φ_r . When $E_{\perp} \approx D$, the observed maximum deflection φ_f increases. For selected values of E_{\perp} , bound states can be temporarily populated.

present (see Fig. 6 and 19a) preventing fair measurement of the rainbow scattering angle. The natural alternative allowing quantitative measurement is to use the standard deviation σ_{ϕ} or its equivalent value σ_{φ} (with $\varphi_f = \arctan(\phi_f/\theta_f)$) which is independent of the projectile energy along x . Fig. 21 reports the evolution of this mean standard scattering width with energy E_{\perp} from the data of the θ -scan plotted in Fig. 6. There is no reason that the value points exactly at the rainbow scattering angle but it is expected to scale in proportion. Fig. 21 shows that σ_{φ} reaches a minimum around 50 meV before displaying a sharp increase at lower values of E_{\perp} . A comparable effect has been observed qualitatively after scattering of helium on a graphene layer⁷⁷ using the HCW or on KCl using a semi-classical approach.⁷⁸ The strategy proposed here is to present the data in a form that is model-independent and which displays a high contrast.

6.7 Quantitative comparison with quantum theory

The comparison of experimental data to theoretical prediction can take different forms depending on which aspect is to be

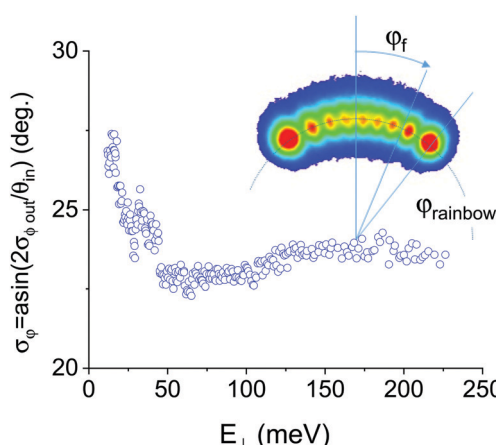


Fig. 21 Evolution of the mean exit angle σ_{φ} (see text) with perpendicular energy E_{\perp} for ${}^4\text{He}$.³³ For each value of k_{\perp} in Fig. 6 (also in Fig. 19b), the width $\sigma_{\varphi f}$ is defined from the width $\sigma_{\varphi f} = \left(\sum_j P(j) \cdot j^2 \phi_B^2 \right)^{1/2}$ where $P(j)$ is the probability distribution of diffraction order j and $\phi_B = \arcsin(G_y/k)$ is the Bragg angle. A clear increase below 50 meV is observed probably due to the refraction effect. Inset shows a typical scattering profile in the semi-classical regime, for $E = 5 \text{ keV}$ and $E_{\perp} = 0.8 \text{ eV}$ where the rainbow angle φ_{rainbow} is indicated.

outlined. When the PEL is calculated without any adjustable parameter the accuracy might not allow a perfect overlap. In this case, qualitative features are searched to point to the possible improvements. This was the case with scattering on GaAs where the PEL obtained by *ab initio* density functional calculations showed a fair agreement only when the attractive forces were scaled down to produce a $D = 8.7 \text{ meV}$ deep potential well before being transformed into diffracted intensities by quantum dynamics calculations. The comparison used to derive the rumpling of the Li^+ ions also relies on a very good qualitative agreement displayed in Fig. 15. This is needed because 2D color plots such as the one in Fig. 12 immediately reinforce the feeling of qualitative agreement. If in addition, a doubt is present, for instance due to an approximate scattering theory, the hope of quantitative comparison rapidly degrades. The other option which became available only recently is to adjust the model to the experimental data. In ref. 35, diffraction data from neon displayed in Fig. 7 and 8 were compared with a recent *ab initio* calculation of the PEL by Miraglia and Gravielle⁷⁹ who kindly accepted to provide a compact description of their results in the form of effective binary interaction potentials. After quantum scattering simulation based on the close coupling code developed by Zugarramurdi and Borisov,³⁶ the comparison with data showed qualitative agreement but also systematic discrepancies. Together with A. G. Borisov a new algorithm was developed with an higher efficiency¹⁰⁶ allowing automatic search of the best fit to the data. Fig. 22 reports the first quantitative agreement of GIFAD data over all diffraction orders and over a significant range of E_{\perp} . The interaction potential derived is therefore an empirical PEL but it can also be seen as a refinement of the initial calculation or a sort of data inversion, probably unique under reasonable initial conditions. A useful application would be to take pure surface electron densities and target positions as calculated using density functional theory and to tune the attractive part and, for instance, the target positions, by optimization of diffraction data.

7 Inelastic diffraction

The previous section, devoted to elastic diffraction, has shown profound similarities between GIFAD and TEAS. We now focus on the differences, among which the ability of GIFAD to observe elastic diffraction at large energy E_{\perp} where the standard Debye-Waller factor would predict negligible elastic intensity. A modified Debye-Waller factor^{56,80} was proposed soon after the first observation even if the first estimations were more a measure of the visibility of the inelastic diffraction since the elastic regime was not demonstrated with GIFAD before 2012.^{18,66} When clear elastic diffraction is observed, the Debye-Waller factor is easily measured as illustrated in Fig. 5b. In this figure, the inelastically scattered intensity shows very well resolved inelastic diffraction peaks corresponding to partially coherent diffraction as modeled in ref. 56. It was rapidly recognized that the thermal movement of surface atoms was responsible for the

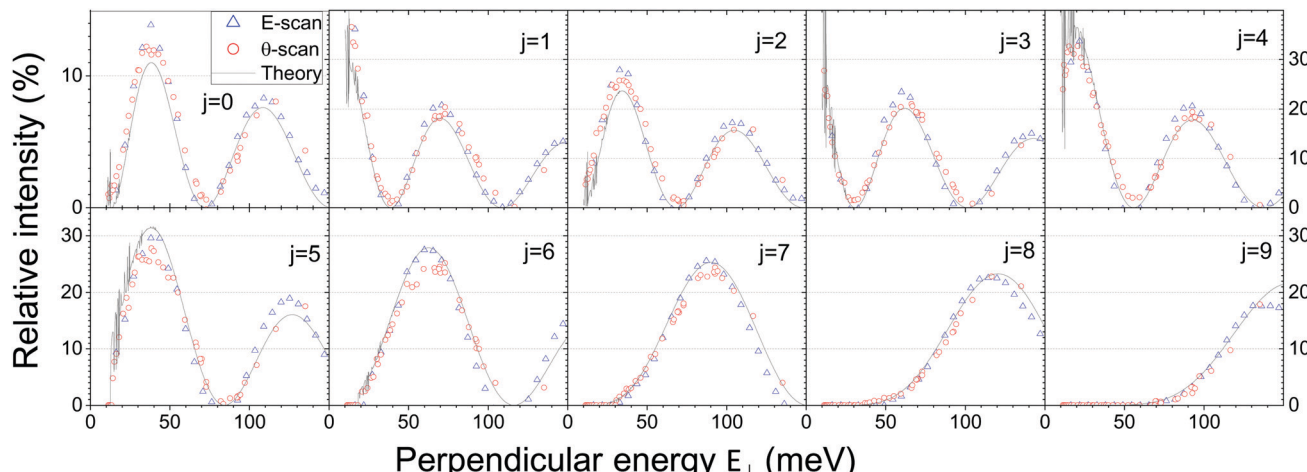


Fig. 22 Neon–LiF (110) diffraction data reported in the θ -scan in Fig. 7 and the E -scan in Fig. 8 are plotted for each diffraction order j , ($\pm j$ added) as a function of the perpendicular energy E_{\perp} . The black line is a calculation using parameterized projectile–surface interaction potential build on the basis of the *ab initio* calculations of ref. 79 optimized to the data by a new close coupling code¹⁰⁶ providing the first quantitative agreement.³⁵

inelastic diffraction but this theory was not readily adapted to GIFAD and early models trying to reproduce thermal effects could qualitatively explain the inelastic scattering profiles but did not account for elastic diffraction,^{31,81,107} leaving some open questions:

- What is the modified DWF?
- What are the inelastic polar and azimuthal profiles?
- What are the inelastic diffraction intensities?

A first attempt to answer these questions was proposed in ref. 57 with the quantum binary collision model (QBCM).

7.1 Classical scattering, momentum transfer, and energy loss

As illustrated in Fig. 2a the projectile trajectory in the (x,y) plane of the fast motion is at the same time very smooth and made of successive localized interaction with individual surface atoms. This local interaction suggests that a binary collision approximation (see *e.g.* ref. 82) can be applied to study the projectile trajectory. The QBCM only introduces a new aspect which is to consider the surface atom as an harmonic oscillator and to consider the collision in the sudden approximation limit. Let us start with elastic scattering. Each target atom is represented by its Debye vibrational wave-function centered at the equilibrium position and, within a sudden approximation, the binary collision transfers a momentum $\delta \vec{k} = m_p \int_{-t_1}^{t_1} \vec{v} dt$ where $t_1 = a_x/2v_x$ is the time needed to cover half the lattice unit a_x along the x direction and $v_x \simeq v$ is the projectile velocity. Assuming a local exponential behavior of the binary effective interaction potential $V_{1D}(z) \propto e^{-rz}$, the momentum transfer is also expected to follow an exponential trend with the minimum distance of approach $\delta k_z \propto e^{-rz}$ producing an equivalent individual deflection angle $\delta\theta = \arcsin(\delta k_z/k)$. Within such simplifying assumptions the trajectory $z(x)$ on the mean 1D potential (V_{1D} in eqn (1)) can be calculated analytically as well as the density of momentum transfer to the surface $dk(x)/dx$. Attributing the momentum transfer to one atom with mass m_t , per lattice unit, the momentum transferred to individual

surface atoms as well as the associated recoil energy $E_r = (\hbar\delta k)^2/2m_t$ can be calculated along the trajectory. The sum ΔE_{Cl} of the recoil momenta $E_r = (\hbar\delta k)^2/2m_t$ with m_t the mass of the recoiling target atom scales as $\Delta E_{\text{Cl}} \propto \theta_i^3$ along a grazing trajectory.^{21,56} Compared with the recoil energy $4\mu E\theta^2$ that would arise from a single binary collision at $2\theta = \theta_i + \theta_f$, ΔE_{Cl} is N_{eff} times smaller,

$$N_{\text{eff}} = \frac{6}{Fa\theta_i}. \quad (6)$$

This number N_{eff} is interpreted as an effective number of binary collision contributed equally by a small deflection $\delta\theta = 2\theta_i/N_{\text{eff}}$. a is the lattice parameter that appears when considering the density of scattering centers on the surface. This result obtained with the mean planar interaction potential was numerically checked to remain valid, for trajectories on a 3D surface with atoms at equilibrium positions. It should be noted that giving an infinite mass to the surface atoms *i.e.* neglecting the recoil energies, the projectile classical scattering falls exactly on a perfect Laue circle outlining the validity of ASCA in the classical regime.^{44,82} Classically, the surface atoms should now be left free to move due to thermal agitation. More precisely their position should display a temperature dependent Gaussian distribution. The scattering profile then becomes much broader with a clear log-normal character (eqn (5)) showing qualitative similarities with observed scattering profiles.^{83,84}

7.2 Quantum binary scattering

The quantum aspect is introduced in the QBCM model by considering the surface atoms as Debye harmonic oscillators. The binary collision with this atom is considered in the sudden approximation and the momentum transfer δk calculated above is interpreted as the momentum transferred to the center of the atomic wave function $|\psi\rangle$ centered at the equilibrium position. In response, the probability that the oscillator undergoes a

vibrational transition can be calculated exactly as $p_e = |\langle \psi | e^{i\delta k z} | \psi \rangle|^2$ which, for an atom initially in the vibrational ground state is proportional to $p_e \propto e^{-E_e/\hbar\omega_D}$ (eqn (3)). This probability is significant only when the recoil energy is less than a vibrational energy quantum²¹ and can be identified as the Mössbauer–Lamb–Dicke probability for recoil-less photon emission characteristic of a trapped atom, for instance in an optical lattice.

Over the complete trajectory, the probability that all individual binary collisions are elastic is the product of all individual probabilities $P_e = \prod p_e$ and factorises as $P_e = e^{-\sum E_i/\hbar\omega_D} = e^{-\Delta E_{\text{el}}/\hbar\omega_D}$. Compared with the standard Debye–Waller factor used in TEAS, a factor N_{eff} appears in the exponent supporting the early interpretation by Rousseau *et al.*⁸⁰ and Manson *et al.*⁵⁶ that the modified Debye–Waller factor adapted to GIFAD can be interpreted as a sharing of the momentum transfer $2k_{iz}$ among N_{eff} equivalent scatterers, explaining the observation of clear elastic diffraction up to a few hundred meV, and well-resolved inelastic Bragg peaks up to a few eV perpendicular energy E_{\perp} .

Of course, the QBCM suffers from imperfections since it neglects attractive forces. This aspect is under development and preliminary results do not contradict this simple approach. More problematic, the eigenstates of the surface vibration modes are not the localized Einstein or Debye modes but the phonon modes as identified in TEAS (see *e.g.* ref. 85). If such a localized vibrational excitation would be inside the bulk, its decomposition to the phonons modes would be an almost perfect dilution since the Fourier transform of a delta function is a white homogeneous distribution.

This might not be the case on a surface where specific vibration modes exist⁸⁶ that are localized close to the surface. Using a slab approach of the surface, Schram and Heller⁸⁷ suggested that the initial excitation could indeed dilute in many phonon modes and that the apparent quasi-elastic diffraction could, in part, be due to the excitation of very low energy mode having a negligible contribution to the angular and energy straggling. It should be noted that, when applied to TEAS, the Lamb–Dicke probability p_e is exactly the Debye–Waller factor suggesting that the vision of a local excitation probability is not fully irrelevant.

7.3 Three different regimes

Each binary collision is either elastic or inelastic but the probability that all N_{eff} equivalent collisions are elastic or inelastic are well separated revealing an intermediate region as illustrated in Fig. 23. On the left-hand side, a quasi-elastic regime can be defined where the overall elastic probability P_e is significant *i.e.* where both elastic and inelastic diffraction should be observed. The effective number of inelastic collisions N_{eff} (eqn (6)) by the probability $p_i = 1 - p_e$ that the collision is inelastic. Fig. 24 shows that this quasi-elastic regime corresponds to at most one inelastic collision with a possible contribution of two collisions when the elastic fraction is below a few percent. The quasi-classical regime is present on the right hand side of the figure where almost all collisions are inelastic

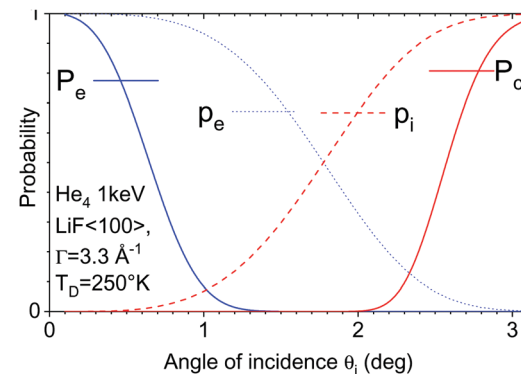


Fig. 23 The probability p_e and $P_c = \prod_{i=1}^{N_{\text{eff}}} p_e$ of individual and overall elastic scattering, respectively. The complementary inelastic probabilities $p_i = (1 - p_e)$ and $P_{ci} = \prod_{i=1}^{N_{\text{eff}}} p_i$ are plotted as a function of the angle of incidence θ_i for 1 keV He.

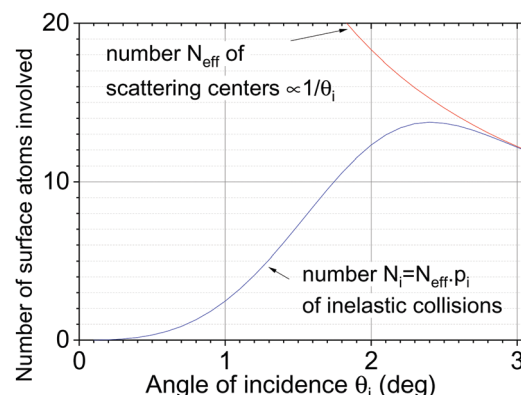


Fig. 24 For the same conditions as Fig. 23, the effective number of scattering centers given by eqn (6) is plotted together with the mean number of inelastic collisions given by $p_i \cdot N_{\text{eff}}$ with $p_i = 1 - p_e$ given by eqn (3).

so that classical simulation should be valid. Note that the perturbative approach proposed here that the resulting angular straggling is simply the sum of individual ones calculated along a common trajectory evaluated on a rigid lattice may reach its limits because the individual deflections are becoming larger and larger as the distance of closest approach decreases. In between lies a broad intermediate region where elastic diffraction is not present and where inelastic diffraction progressively blurs but where classical simulation models might fail because the quantum features should continue to play a role.

7.4 Inelastic scattering

The second aspect of the QBCM is to propose a perturbative strategy to evaluate the energy and angular straggling associated with an inelastic collision. If the collision is elastic then the target atom wave function $|\psi\rangle$ is left unchanged and the transferred momentum δk leaves no possibility to localize the target atom. At variance, if the collision is inelastic, all possible

vibrational excitation should be calculated together with the associated momentum transfer. The QBCM empirically considers that the classical description of collision is a good approximation of the angular and energy straggling. The target atom wave-function $|\psi\rangle$ centred at equilibrium is then replaced by its position probability distribution $|\langle\psi|\vec{r}|\psi\rangle|^2$. For a harmonic oscillator at temperature T , this distribution is a Gaussian function with a standard deviation given by eqn (4). Each value of \vec{r} produces a specific deflection angle. Restricting here to target movement along z , a displacement from equilibrium by δz gives a scattering angle $\delta\theta = e^{-\Gamma(z+\delta z)}$. When weighted by the Gaussian probability distribution of z this produces a log-normal distribution (eqn (5)) centered around the elastic value $\delta\theta_e = e^{-\Gamma z}$. The relative width $w = \delta\theta/\theta_i = \Gamma\sigma$ is independent of the angle of incidence θ_i . Considering that the thermal variation δz is much smaller than the distance z of the projectile to the surface atom, the QBCM suggests a statistical treatment of the angular and energy straggling *i.e.* that the variance of the polar inelastic scattering distribution is the sum of the variance of all inelastic events.

7.5 Azimuthal and polar profiles

The QBCM evaluates the inelastic momentum transfer from classical trajectories. The mean classical trajectory evaluated from the mean interaction potential $V_{1D}(z)$ is enough to obtain significant values for the elastic and inelastic scattering probabilities but has no chance to provide a quantitative estimate of the lateral and polar shapes $\delta\phi_f$ of the inelastic diffraction peaks. When the collision is considered inelastic, we consider the 3D classical distribution. This alone does not produce a very large broadening if only the ‘on-top’ trajectories are considered. To evaluate all conditions for binary collisions, the momentum exchange leading to inelastic effects have to be averaged over all impact parameter inside the lattice unit. Each inelastic event provides a radial momentum transfer oriented along the inter-nuclear axis and all contributions are added to generate individual inelastic scattering. These are then self convoluted as many times as the number of inelastic events.

The three coordinates of the atom wave-function $|\psi\rangle$ centred at equilibrium are replaced by their position probability distribution $|\langle\psi|\vec{r}|\psi\rangle|^2$. This is true also for the polar profile. The model described above predicts a log-normal distribution but only for a single collision and for an “on top” binary collision. For multiple collisions, the polar inelastic profile should be a convolution of such log-normal distributions and though such convolution is not a log-normal profile in general the numerical convolutions turned out to keep a very strong log-normal character, probably because the relative width parameter w is small (*e.g.* $w = 0.06$ in Fig. 5b). Still, “on top” collisions are specific and transfer momentum mainly along the z direction. Taking into account a reasonable value of the inelastic momentum transfer $\delta\vec{k}$ induced by an inelastic collision with a surface atom at a given location with respect to the projectile, classical trajectories are needed. This is however comparatively easy because only a lattice site has to be inspected to evaluate the vectorial aspect of the momentum transfer. This has been

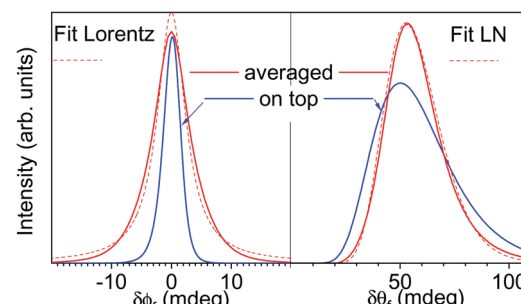


Fig. 25 Angular straggling σ_{θ_f} (right) and σ_{ϕ_f} (left) of an individual inelastic collision averaged over the lattice cell.²¹ Compared with the “on-top” trajectory, the lateral broadening has acquired a partial Lorentzian character while the log-normal scale parameter $w \sim \sigma_{\phi_f}/\theta_s$ describing the broadening of the polar distribution is reduced by $\approx 30\%$.

done for LiF^{21,57} and Fig. 25 shows that the resulting polar profile maintains a log-normal character although with a width reduced by 30% while the azimuthal width becomes larger acquiring large tails but significantly less than a pure Lorentzian profile as derived by Seifert *et al.*²⁶ for the combination of elastic and inelastic contributions. The excessive width of the Lorentzian profile was shown to produce errors in the deconvolution of purely inelastic diffraction, away from the Laue circle.²¹

7.6 Inelastic profiles in E -scan and θ -scan

Regarding inelastic diffraction the ASCA is not valid anymore and the energy E_\perp is no longer a good quantum number. As an illustration, the E -scan of Fig. 8 and θ -scan of Fig. 7 which have similar elastic diffracted intensities when plotted as a function of E_\perp (Fig. 22) have very different inelastic scattering widths. This latter is determined as the line profile providing a good fit of the inelastic diffracted intensities as illustrated in the bottom of Fig. 18. To first order, the inelastic line-width was found almost constant during the E -scan while, it was found to increase almost linearly with E_\perp during the θ -scan.²⁶ In both cases, diffraction progressively disappears as the inelastic line-width σ_{ϕ_f} compares with the Bragg angle ϕ_B which behave exactly opposite; constant during a θ -scan and decreasing with \sqrt{E} in an E -scan. During an E -scan, the projectile trajectory is essentially unchanged and it is only shifted closer to the surface as the energy E_\perp increases. The effective number of collisions N_{eff} is constant as well as the overall elastic deflection angle $\theta_i + \theta_f$ and the individual elastic deflection angle $\delta\theta_f = 2\theta_f/N_{\text{eff}}$. According to the QBCM, each inelastic collision has a log-normal angular distribution characterized by a constant ratio w between the elastic scattering angle and the inelastic broadening (eqn (5)) so that, in the quasi-elastic regime, the polar and azimuthal inelastic profiles are expected to remain constant during an E -scan. During a θ -scan, the number of binary collisions decreases with the angle of incidence θ_i (eqn (6)) while the overall deflection increases so that each binary collision is associated with individual elastic deflection angles $\delta\theta_s$ scaling with θ_i^2 , *i.e.* with E_\perp in a θ -scan.

7.7 Why inelastic is almost like the elastic

When analyzing the diffraction images, *e.g.* in Fig. 5b, it was noted that in spite of a sharp variation of the absolute intensity, the diffracted relative intensities above and below the Laue circle are different but show a perfect continuity with the elastic one. To interpret these inelastic diffracted intensities a wavelength is needed. It was found experimentally^{21,58} that using the half sum $k_{\text{eff}} = (k_{i\perp} + k_{f\perp})/2$ also offers a continuity in the data analysis. The inelastic diffracted intensities measured at k_{eff} closely match the elastic diffracted intensities measured at the same value of $k_{i\perp} = k_{\text{eff}}$ provided that k_{eff} is chosen within the fwhm of the inelastic scattering distribution *i.e.* not too far from specular.

Within the QBCM, this can be explained in the quasi-elastic regime where, on average, only one inelastic collision is responsible for each event of the inelastic profile. The blue peaks in the trajectory in Fig. 2 correspond to the acceleration γ_z and their integral correspond to the momentum transfer to the surface atoms. The recoil energy E_r should scale as the square of these values producing a distribution well-localized around the turning point of the trajectory where the distance z to the surface is minimum. The inelastic probability $p_i = 1 - p_e$ can be expended as $p_i \sim E_r/\hbar\omega$ and is also expected to be localized around the turning point so that a typical inelastic event would consist of two half elastic trajectories with the surface, the way-in with a wave-number k_i and a way-out with a wave-number k_f . In between a single inelastic event provides a small additional kick to the momentum change accumulated in both half collisions. The evolution of the elastic intensities displayed in diffraction charts (*e.g.* in Fig. 7) explains why the inelastic diffraction appears as directed mainly upward or downward at different diffraction orders or different values of E_\perp as in Fig. 4. The thermal distribution of these kicks along the y and z directions is displayed in Fig. 25 and the diffraction remains visible as long as this or these additional kicks along y are less than a reciprocal lattice vector.

Table 2 indicates the important scaling laws appearing in GIFAD. Except for the first two items, all quantities have the primary energy $E \sim 10^3$ eV as a pre-factor, however, for an angle of incidence $\theta_i = 0.5^\circ \sim 10^{-2}$ rad, the successive powers of θ_i allow, for instance, recoil energy E_r in the meV range. Attention should be paid that these scaling laws do not take into account the attractive part of the potential and become irrelevant for energies $E_\perp \leq D$ where D would be the depth of the attractive

Table 2 Scaling laws, the magnification/amplification factor corresponds to $\theta = 0.5^\circ \simeq 10^{-2}$ rad

L	Trajectory length	θ^{-1}	10^2
N_{eff}	Effective number of scatterer	θ	10^{-2}
ΔE_b	Gas phase binary recoil energy	θ^2	10^{-4}
ΔE_{Cl}	Classical projectile energy loss	θ^3	10^{-6}
P_i	Inelastic projectile scattering probability	θ^3	10^{-6}
E_r	Individual recoil energy	θ^4	10^{-8}
p_i	Individual inelastic probability	θ^4	10^{-8}
ΔE_{qu}	Mean quantum projectile energy loss	θ^7	10^{-14}
E_{rqu}	Mean quantum individual recoil energy	θ^8	10^{-16}

well, if any. Additional work is needed to turn the inelastic model quantitative so that it can be exploited to derive surface Debye temperature or electron–phonon coupling,⁸⁸ or, reversely, the absolute surface temperature, a key parameter during growth processes. So far it has not been possible with GIFAD to identify specific phonon modes by inelastic diffraction but a better understanding would probably help in tracking the signs of surface vibrations.

8 Applications of GIFAD

The present paper is focused on academic systems of rare gases diffracted by the LiF surface but fast atom diffraction has been observed on metals such as Ag⁸⁹ and Ni⁹⁰ and semi-conductors ZnSe⁵² and GaAs.³⁴ Due to the grazing geometry identical to that of RHEED, GIFAD has shown to be compatible with the MBE environment where it is mandatory to leave the space facing the surface free of any instrument to allow well-controlled evaporation.⁶⁸

In this context, GIFAD was able to follow *in situ* and online the growth process with pronounced intensity oscillations having a maximum for each layer completion whatever the angles of incidence θ_i or ϕ_i , and whatever the primary energy.⁹¹ This simplicity is due to the absence of any penetration below the topmost layer so that no inter-layer interference cannot modify the natural oscillation of the reflectivity during the completion of a new layer. Fig. 26 shows that almost all scattering parameters oscillate, the intensity, the mean scattering angle and the polar width. Similar oscillations of the specular intensity were observed with ions where diffraction does not show up (see *e.g.* ref. 92). GIFAD simply provides an additional extremely detailed view of the surface topology and reconstruction before growth to keep track of the starting conditions as well as after growth to qualify the final layer.

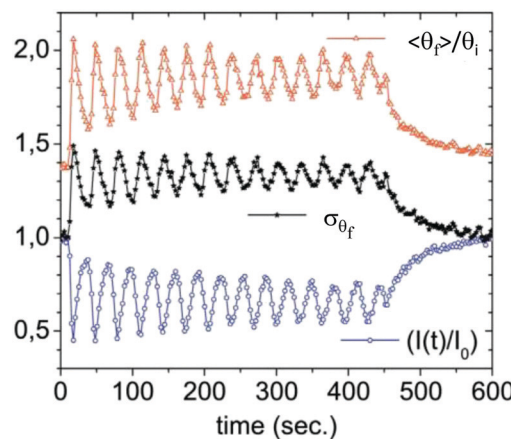


Fig. 26 Time evolution of the intensity $I(t)/I_0$, on the Laue circle, of the mean scattering angle $\langle \theta_f \rangle$ and of the scattering width σ_{θ_f} during a homoepitaxial, layer by layer growth of GaAs on GaAs inside a MBE chamber.^{68,91} The intensity on the Laue circle is maximum at each layer completion while σ_{θ_f} and $\langle \theta_f \rangle$ are maximum in between indicating that the intensity missing at the Laue circle is mainly scattered at a larger angle when the flatness of the surface reduces.

Table 3 The following abbreviations are used in this manuscript

FAD	Fast atom diffraction
FWHM	Full width at half maximum
GIFAD	Grazing incidence fast atom diffraction
HAS	Helium atom scattering
HCW	Hard corrugated wall
LEED	Low energy electron diffraction
MBE	Molecular beam epitaxy
PEL (or PES)	Potential energy landscape (or surface)
QBCM	Quantum binary collision model
RHEED	Reflection high energy electron diffraction
TEAS	Thermal energy atom scattering

In general, the surface sensitivity is extreme, in the sense that, like TEAS, fast atom diffraction takes place a few Å above the terminal layer so that the diffraction images are not contaminated by information originating from the bulk. This top most layer sensitivity is of great importance to investigate the surface reconstructions triggered by temperature,³⁴ by oxygen adsorption⁹³ or by migration of contaminants,⁹⁴ single over-layers of organic⁹⁵ or inorganic insulating⁹⁶ and conducting^{77,97} materials and ultra thin films in general. GIFAD does not induce any charging of the surface and should be compatible with the situation where a large electric or magnetic field is present.

8.1 Perspective

From the fundamental point of view, the inelastic diffraction is an important challenge, and collaboration is needed with TEAS where several theoretical approaches^{86,98,99} have been developed to encompass both elastic and inelastic diffraction. Experimentally, a combined GIFAD and HAS study of a thin overlayer, for instance of graphene,¹⁰⁰ would probably help in the identification of specific vibration modes and allow significant progress. Regarding elastic diffraction, the recent progress³⁵ should allow for the implementation of a crystallographic software starting with a qualitative adjustment of surface atoms coordinates and effective binary interaction potentials by the HCW model and then final quantitative optimization by quantum scattering programs.

9 Conclusions

Due to the very efficient decoupling of the movement perpendicular and parallel to the surface, GIFAD is a variable energy diffraction technique, where E_{\perp} can be tuned between a few meV up to eV. This large energy range gives access to the physisorption regime where the depth of the attractive potential energy well can be determined and on the other side to the structural regime where atomic positions can be determined with a few pm accuracy and charge transfer processes are easily measured. It seems difficult to reach significantly lower values, such as those needed for quantum reflection¹⁰¹ but an extension to semi-classical and classical regimes is comparatively easy, allowing complementary measurements such as the direct recoil spectrometry^{102,103} providing identification of surface contaminants. The theoretical description of the elastic regime has made significant progress so that the

experimental data can now be fitted to a potential energy landscape making the corrugation function a subsidiary output with practical interest but moderate significance. The inelastic regime is much less advanced but is making rapid progress and should help to diagnose imperfect situations such as those encountered during the growth process. Finally, one regret, obvious but sincere, is that we would have liked to visit our honored guest J. P. Toennies soon after GIFAD was discovered.

Conflicts of interest

There are no conflicts to declare.

Acknowledgements

The authors are indebted to all the students and colleagues who took part in the experiments and interpretations, V. A. Morosov, A. Kalinin, Z. Szilagyi, J. Villette, and J. P. Atanas who constructed the original setup equipped with a position-sensitive detector facing the beam where GIFAD was discovered and P. Rousseau, Y. Xiang, P. Soulisse, L. Boubekeur, M. Mullier, A. Momeni, N. Bundaleski, N. Kalashnyk, H. Khemliche, J. S. Alarcón, P. Lunca-popa, Z. Mu, M. Sereno, and L. Lavoine who took part in the discovery and investigations with fast atom diffraction at Orsay. We are grateful to H. Remita from the Institut de Chimie Physique at Orsay (France) for irradiating our LiF crystals by γ -rays allowing a very large mean terrace size after cleaving. We acknowledge the continuous and enlightening discussions with A. G. Borisov, A. Zugarramurdi, J. R. Manson and M. S. Gravielle. Finally, one of the authors would like to give tribute to the late Michel Barat¹⁰⁴ who trained him to atomic collision with great enthusiasm. This work has been funded by the French Agence Nationale de la Recherche (ANR-07-BLAN-0160, ANR-2011-EMMA-003-01 and ANR-10-LABX-0039-PALM).

Notes and references

- U. Harten, A. M. Lahee, J. P. Toennies and C. Wöll, Observation of a soliton reconstruction of Au(111) by high-resolution helium-atom diffraction, *Phys. Rev. Lett.*, 1985, **54**, 2619–2622.
- H.-J. Ernst, F. Fabre, R. Folkerts and J. Lapujoulade, Observation of a growth instability during low temperature molecular beam epitaxy, *Phys. Rev. Lett.*, 1994, **72**, 112.
- G. Boato, P. Cantini and L. Mattera, A study of the (001)LiF surface at 80 K by means of diffractive scattering of He and Ne atoms at thermal energies, *Surf. Sci.*, 1976, **55**(1), 141–178.
- T. Engel and K. Rieder, Structural studies of surfaces with atomic and molecular beam diffraction, *Springer Tracts in Modern Physics*, 1982, vol. 91, pp. 55–180.
- H. Hoinkes, The physical interaction potential of gas atoms with single-crystal surfaces, determined from gas-surface diffraction experiments, *Rev. Mod. Phys.*, 1980, **52**, 933–970.

- 6 D. R. Frankl, Atomic beam scattering from single crystal surfaces, *Prog. Surf. Sci.*, 1983, **13**(4), 285–355.
- 7 J. Barker and D. Auerbach, Gas–surface interactions and dynamics; thermal energy atomic and molecular beam studies, *Surf. Sci. Rep.*, 1984, **4**(1), 1–99.
- 8 D. Farias and K. Rieder, Atomic beam diffraction from solid surfaces, *Rep. Prog. Phys.*, 1998, **61**(12), 1575–1664.
- 9 B. Gumhalter, Single- and multiphonon atom-surface scattering in the quantum regime, *Phys. Rep.*, 2001, **351**(1), 1–159.
- 10 G. Benedek and J. P. Toennies, *Atomic Scale Dynamics at Surfaces*, Springer Series in Surface Science, Springer, 2018.
- 11 P. Rousseau, H. Khemliche, A. G. Borisov and P. Roncin, Quantum scattering of fast atoms and molecules on surfaces, *Phys. Rev. Lett.*, 2007, **98**, 016104.
- 12 H. Khemliche, P. Rousseau and P. Roncin, *Device and method for characterizing surfaces*, 2006.
- 13 A. Schüller, S. Wethekam and H. Winter, Diffraction of fast atomic projectiles during grazing scattering from a LiF(001) surface, *Phys. Rev. Lett.*, 2007, **98**, 016103.
- 14 V. A. Morosov, A. Kalinin, Z. Szilagyi, M. Barat and P. Roncin, 2π spectrometer: a new apparatus for the investigation of ion surface interaction, *Rev. Sci. Instrum.*, 1996, **67**(6), 2163–2170.
- 15 M. Mannami, K. Kimura, K. Nakanishi and A. Nishimura, Glancing-angle scattering of fast ions at solid surfaces, *Nucl. Instrum. Methods Phys. Res., Sect. B*, 1986, **13**(1), 587–593.
- 16 E. Andreev, Quantum and classical characteristics of glancing scattering of fast atoms on the surface of a crystal, *Russ. J. Phys. Chem. A*, 2002, **76**, 164–169.
- 17 P. Maksym and J. Beeby, A theory of RHEED, *Surf. Sci.*, 1981, **110**(2), 423–438.
- 18 M. Busch, J. Seifert, E. Meyer and H. Winter, Evidence for longitudinal coherence in fast atom diffraction, *Phys. Rev. B: Condens. Matter Mater. Phys.*, 2012, **86**, 241402.
- 19 A. Zugarramurdi and A. G. Borisov, When fast atom diffraction turns 3D, *Nucl. Instrum. Methods Phys. Res., Sect. B*, 2013, **317**, 83–89.
- 20 A. Zugarramurdi, M. Debiossac, P. Lunca-Popa, L. S. Alarcón, A. Momeni, H. Khemliche, P. Roncin and A. G. Borisov, Surface-grating deflection of fast atom beams, *Phys. Rev. A: At., Mol., Opt. Phys.*, 2013, **88**, 012904.
- 21 P. Roncin and M. Debiossac, Elastic and inelastic diffraction of fast atoms, Debye-Waller factor, and Mössbauer-Lamb-Dicke regime, *Phys. Rev. B*, 2017, **96**, 035415.
- 22 H. Winter and A. Schüller, Fast atom diffraction during grazing scattering from surfaces, *Prog. Surf. Sci.*, 2011, **86**(9), 169–221.
- 23 C. Henkel, J.-Y. Courtois and A. Aspect, Atomic diffraction by a thin phase grating, *J. Phys. II*, 1994, **4**(11), 1955–1974.
- 24 D. Farias, C. Diaz, P. Nieto, A. Salin and F. Martin, Pronounced out-of-plane diffraction of H₂ molecules from a Pd(111) surface, *Chem. Phys. Lett.*, 2004, **390**(1), 250–255.
- 25 P. Rousseau, H. Khemliche and P. Roncin, Auger rates on NaCl(001), effect of the final state and modeling via an effective length, *Nucl. Instrum. Methods Phys. Res., Sect. B*, 2007, **258**(1), 13–17.
- 26 J. Seifert, J. Lienemann, A. Schüller and H. Winter, Studies on coherence and decoherence in fast atom diffraction, *Nucl. Instrum. Methods Phys. Res., Sect. B*, 2015, **350**, 99–105.
- 27 M. S. Gravielle and J. E. Miraglia, Influence of beam collimation on fast-atom diffraction studied via a semi-quantum approach, *Phys. Rev. A: At., Mol., Opt. Phys.*, 2015, **92**, 062709.
- 28 J. J. Gilman, C. Knudsen and W. P. Walsh, Cleavage cracks and dislocations in LiF crystals, *J. Appl. Phys.*, 1958, **29**(4), 601–607.
- 29 J. Lapington, A comparison of readout techniques for high-resolution imaging with microchannel plate detectors, *Nucl. Instrum. Methods Phys. Res., Sect. A*, 2004, **525**(1), 361–365.
- 30 S. Lupone, P. Soulisse and P. Roncin, A large area high resolution imaging detector for fast atom diffraction, *Nucl. Instrum. Methods Phys. Res., Sect. B*, 2018, **427**, 95–99.
- 31 F. Aigner, N. Simonović, B. Solleeder, L. Wirtz and J. Burgdörfer, Suppression of decoherence in fast-atom diffraction at surfaces, *Phys. Rev. Lett.*, 2008, **101**, 253201.
- 32 A. Schüller, S. Wethekam, D. Blauth, H. Winter, F. Aigner, N. Simonović, B. Solleeder, J. Burgdörfer and L. Wirtz, Rumpling of LiF(001) surface from fast atom diffraction, *Phys. Rev. A: At., Mol., Opt. Phys.*, 2010, **82**, 062902.
- 33 M. Debiossac, A. Zugarramurdi, P. Lunca-Popa, A. Momeni, H. Khemliche, A. G. Borisov and P. Roncin, Transient quantum trapping of fast atoms at surfaces, *Phys. Rev. Lett.*, 2014, **112**, 023203.
- 34 M. Debiossac, A. Zugarramurdi, H. Khemliche, P. Roncin, A. G. Borisov, A. Momeni, P. Atkinson, M. Eddrief, F. Finocchi and V. H. Etgens, Combined experimental and theoretical study of fast atom diffraction on the $\beta_2(2 \times 4)$ reconstructed GaAs(001) surface, *Phys. Rev. B: Condens. Matter Mater. Phys.*, 2014, **90**, 155308.
- 35 M. Debiossac, P. Roncin and A. G. Borisov, Refraction of fast Ne atoms in the attractive well of a LiF(001) surface, *J. Phys. Chem. Lett.*, 2020, **11**(12), 4564–4569 PMID: 32421332.
- 36 A. Zugarramurdi and A. G. Borisov, Transition from fast to slow atom diffraction, *Phys. Rev. A: At., Mol., Opt. Phys.*, 2012, **86**, 062903.
- 37 A. Muzas, F. Gatti, F. Martín and C. Díaz, Diffraction of H from LiF(001): From slow normal incidence to fast grazing incidence, *Nucl. Instrum. Methods Phys. Res., Sect. B*, 2016, **382**, 49–53.
- 38 A. S. Sanz, F. Borondo and S. Miret-Artés, Causal trajectories description of atom diffraction by surfaces, *Phys. Rev. B: Condens. Matter Mater. Phys.*, 2000, **61**, 7743–7751.
- 39 A. S. Sanz and S. Miret-Artés, A trajectory-based understanding of quantum interference, *J. Phys. A: Math. Theor.*, 2008, **41**, 435303.
- 40 M. del Cueto, A. Muzas, F. Martín and C. Díaz, Accurate simulations of atomic diffractive scattering from KCl(001)

- under fast grazing incidence conditions, *Nucl. Instrum. Methods Phys. Res., Sect. B*, 2020, **476**, 1–9.
- 41 A. Schüller, D. Blauth, J. Seifert, M. Busch, H. Winter, K. Gärtner, R. Włodarczyk, J. Sauer and M. Sierka, Fast atom diffraction during grazing scattering from a MgO(001) surface, *Surf. Sci.*, 2012, **606**(3), 161.
 - 42 M. S. Gravielle and J. E. Miraglia, Quantum interference in grazing scattering of swift He atoms from LiF(001) surfaces: Surface eikonal approximation, *Nucl. Instrum. Methods Phys. Res., Sect. B*, 2009, **267**(4), 610–614.
 - 43 M. Gravielle, A. Schüller, H. Winter and J. Miraglia, Fast atom diffraction for grazing scattering of Ne atoms from a LiF(001) surface, *Nucl. Instrum. Methods Phys. Res., Sect. B*, 2011, **269**(11), 1208.
 - 44 D. M. Danailov and D. S. Karpuzov, Total reflection of energetic ions from crystal surfaces at glancing incidence, *Can. J. Phys.*, 1997, **75**(4), 197–209.
 - 45 M. S. Gravielle and J. E. Miraglia, Semiquantum approach for fast atom diffraction: Solving the rainbow divergence, *Phys. Rev. A: At., Mol., Opt. Phys.*, 2014, **90**(5), 052718.
 - 46 G. Bocan and M. Gravielle, Gifad for he/KCl(001). structure in the pattern for $\langle 110 \rangle$ incidence as a measure of the projectile-cation interaction, *Nucl. Instrum. Methods Phys. Res., Sect. B*, 2018, **421**, 1.
 - 47 G. Armand and J. R. Manson, Scattering of neutral atoms by an exponential corrugated potential, *Phys. Rev. Lett.*, 1979, **43**, 1839–1842.
 - 48 U. Garibaldi, A. Levi, R. Spadacini and G. Tommei, Quantum theory of atom-surface scattering: Diffraction and rainbow, *Surf. Sci.*, 1975, **48**(2), 649–675.
 - 49 G. Armand and J. R. Manson, Scattering by a hard corrugated wall: An exact solution, *Phys. Rev. B: Condens. Matter Mater. Phys.*, 1978, **18**, 6510–6518.
 - 50 G. Armand and J. Manson, Elastic and inelastic scattering of neutral atoms by a corrugated hard wall, *Surf. Sci.*, 1979, **80**, 532–542.
 - 51 A. Momeni, P. Soulisse, P. Rousseau, H. Khemliche and P. Roncin, Grazing incidence fast atom diffraction (gifad): Doing rheed with atoms, *eJ. Surf. Sci. Nanotechnol.*, 2010, **8**, 101–104.
 - 52 H. Khemliche, P. Rousseau, P. Roncin, V. H. Etgens and F. Finocchi, Grazing incidence fast atom diffraction: An innovative approach to surface structure analysis, *Appl. Phys. Lett.*, 2009, **95**(15), 151901.
 - 53 P. Roncin, J. Villette, J. P. Atanas and H. Khemliche, Energy loss of low energy protons on lif(100): surface excitation and H^- mediated electron emission, *Phys. Rev. Lett.*, 1999, **83**, 864–867.
 - 54 J. Lienemann, A. Schüller, D. Blauth, J. Seifert, S. Wethekam, M. Busch, K. Maass and H. Winter, Coherence during scattering of fast H atoms from a LiF(001) surface, *Phys. Rev. Lett.*, 2011, **106**, 067602.
 - 55 P. Rousseau, *Collisions rasantes d'ions ou d'atomes sur les surfaces: de l'échange de charge à la diffraction atomique*, PhD thesis, Université Paris Sud –XI Paris, 2006.
 - 56 J. R. Manson, H. Khemliche and P. Roncin, Theory of grazing incidence diffraction of fast atoms and molecules from surfaces, *Phys. Rev. B: Condens. Matter Mater. Phys.*, 2008, **78**, 155408.
 - 57 P. Roncin, M. Debiossac, H. Oueslati and F. Raouafi, Energy loss and inelastic diffraction of fast atoms at grazing incidence, *Nucl. Instrum. Methods Phys. Res., Sect. B*, 2018, **427**, 100–107.
 - 58 M. Debiossac and P. Roncin, Image processing for grazing incidence fast atom diffraction, *Nucl. Instrum. Methods Phys. Res., Sect. B*, 2016, **382**, 36.
 - 59 J. Seifert, A. Schüller, H. Winter and K. Gärtner, Transition from axial to planar surface channeling for fast atom diffraction, *Nucl. Instrum. Methods Phys. Res., Sect. B*, 2011, **269**(11), 1212–1215.
 - 60 F. E. Feiten, J. Seifert, J. Paier, H. Kuhlenbeck, H. Winter, J. Sauer and H.-J. Freund, Surface structure of $V_2O_3(0001)$ revisited, *Phys. Rev. Lett.*, 2015, **114**, 216101.
 - 61 N. Kalashnyk, H. Khemliche and P. Roncin, Atom beam triangulation of organic layers at 100mev normal energy: self-assembled perylene on Ag(110) at room temperature, *Appl. Surf. Sci.*, 2016, **364**, 235–240.
 - 62 M. Debiossac and P. Roncin, Atomic diffraction under oblique incidence: An analytical expression, *Phys. Rev. A: At., Mol., Opt. Phys.*, 2014, **90**, 054701.
 - 63 A. Ruiz, J. P. Palao and E. J. Heller, Classical and quantum analysis of quasiresonance in grazing atom-surface collisions, *Phys. Rev. A: At., Mol., Opt. Phys.*, 2009, **79**, 052901.
 - 64 E. Pollak and S. Miret-Artés, Second-order semiclassical perturbation theory for diffractive scattering from a surface, *J. Phys. Chem. C*, 2015, **119**(12), 14532.
 - 65 M. Sereno, S. Lupone, M. Debiossac, N. Kalashnyk and P. Roncin, Active correction of the tilt angle of the surface plane with respect to the rotation axis during azimuthal scan, *Nucl. Instrum. Methods Phys. Res., Sect. B*, 2016, **382**, 123–126.
 - 66 B. Lalmi, H. Khemliche, A. Momeni, P. Soulisse and P. Roncin, High resolution imaging of superficial mosaicity in single crystals using grazing incidence fast atom diffraction, *J. Phys.: Condens. Matter*, 2012, **24**, 442002.
 - 67 R. Pfandzelter, T. Bernhard and H. Winter, Ion beam triangulation of ultrathin Mn and comn films grown on Cu(001), *Phys. Rev. Lett.*, 2003, **90**, 036102.
 - 68 M. Debiossac, P. Atkinson, A. Zugarramurdi, M. Eddrief, F. Finocchi, V. Etgens, A. Momeni, H. Khemliche, A. Borisov and P. Roncin, Fast atom diffraction inside a molecular beam epitaxy chamber, a rich combination, *Appl. Surf. Sci.*, 2017, **391**, 53–58.
 - 69 A. Schüller and H. Winter, Supernumerary rainbows in the angular distribution of scattered projectiles for grazing collisions of fast atoms with a LiF(001) surface, *Phys. Rev. Lett.*, 2008, **100**, 097602.
 - 70 A. Schüller, H. Winter, M. S. Gravielle, J. M. Pruneda and J. E. Miraglia, He-LiF surface interaction potential from fast atom diffraction, *Phys. Rev. A: At., Mol., Opt. Phys.*, 2009, **80**, 062903.
 - 71 U. Specht, M. Busch, J. Seifert, A. Schüller, H. Winter, K. Gärtner, R. Włodarczyk, M. Sierka and J. Sauer, Rainbow

- Published on 06 January 2021. Downloaded by Chalmers Tekniska Högskola on 3/20/2023 7:52:24 PM.
- scattering under axial surface channeling from a KCl(001) surface, *Phys. Rev. B: Condens. Matter Mater. Phys.*, 2011, **84**, 125440.
- 72 L. Frisco, J. E. Miraglia and M. S. Gravielle, Spot-beam effect in grazing atom-surface collisions: from quantum to classical, *J. Phys.: Condens. Matter*, 2018, **30**(40), 405001.
- 73 R. Grisenti, W. Schöllkopf, J. Toennies, C. Hegerfeldt and T. Kohler, Determination of atom-surface van der Waals potentials from transmission-grating diffraction intensities, *Phys. Rev. Lett.*, 1999, **83**, 1755–1758.
- 74 A. P. Jardine, S. Dworski, P. Fouquet, G. Alexandrowicz, D. J. Riley, G. Y. H. Lee, J. Ellis and W. Allison, Ultrahigh-resolution spin-echo measurement of surface potential energy landscapes, *Science*, 2004, **304**(5678), 1790.
- 75 R. Frisch and O. Stern, Anomalien bei der spiegelnden reflection und beugung von molekularstrahlen an kristall-spaltflächen, *Z. Phys.*, 1933, **84**(7), 430.
- 76 E. Semerad, P. Sequard-Base and E. Hörl, Resonant scattering of Ne/LiF(001) measured by time of flight analysis, *Surf. Sci.*, 1987, **189–190**, 975–983.
- 77 M. Debiossac, A. Zugarramurdi, Z. Mu, P. Lunca-Popa, A. J. Mayne and P. Roncin, Helium diffraction on sic grown graphene: Qualitative and quantitative descriptions with the hard-corrugated-wall, *Phys. Rev. B*, 2016, **94**, 205403.
- 78 G. Bocan, H. Breiss, A. Szilasi, S. Momeni, E. M. Staicu-Casagrande, M. Gravielle, E. Sánchez and H. Khemliche, Anomalous KCl(001) Surface Corrugation from Fast He Diffraction at Very Grazing Incidence, *Phys. Rev. Lett.*, 2020, **125**, 096101.
- 79 J. E. Miraglia and M. S. Gravielle, Reexamination of the interaction of atoms with a lif(001) surface, *Phys. Rev. A*, 2017, **95**, 022710.
- 80 P. Rousseau, H. Khemliche, N. Bundaleski, P. Soulisse, A. Momeni and P. Roncin, Surface analysis with grazing incidence fast atom diffraction (GIFAD), *J. Phys.: Conf. Ser.*, 2008, **133**, 012013.
- 81 L. Frisco and M. S. Gravielle, Phonon contribution in grazing-incidence fast atom diffraction from insulator surfaces, *Phys. Rev. A*, 2019, **100**, 062703.
- 82 G. Hobler and K. Nordlund, Channeling maps for Si ions in Si: Assessing the binary collision approximation, *Nucl. Instrum. Methods Phys. Res., Sect. B*, 2019, **449**, 17–21.
- 83 R. Pfandzelter, T. Hecht and H. Winter, Angular straggling in grazing scattering of fast he-atoms from an Al(111)-surface, *Europhys. Lett.*, 1998, **44**, 116.
- 84 J. Villette, A. G. Borisov, H. Khemliche, A. Momeni and P. Roncin, Subsurface-channeling-like energy loss structure of the skipping motion on an ionic crystal, *Phys. Rev. Lett.*, 2000, **85**, 3137–3140.
- 85 D. Eichenauer and J. P. Toennies, Theory of resonant inelastic one-phonon scattering of he atoms from a LiF(001) single crystal surface, *J. Chem. Phys.*, 1986 **85**, 532.
- 86 G. Benedek, S. Miret-Artés, J. R. Manson, A. Ruckhofer, W. E. Ernst and A. Tamtögl, Origin of the electron-phonon interaction of topological semimetal surfaces measured with helium atom scattering, *J. Phys. Chem. Lett.*, 2020, **11**(5), 1927.
- 87 M. C. Schram and E. J. Heller, Approach to coherent interference fringes in helium-surface scattering, *Phys. Rev. A*, 2018, **98**, 022137.
- 88 A. Tamtögl, P. Kraus, N. Avidor, M. Bremholm, E. M. J. Hedegaard, B. B. Iversen, M. Bianchi, P. Hofmann, J. Ellis, W. Allison, G. Benedek and W. E. Ernst, Electron-phonon coupling and surface Debye temperature of Bi₂Te₃(111) from helium atom scattering, *Phys. Rev. B*, 2017, **95**(19), 195401.
- 89 N. Bundaleski, H. Khemliche, P. Soulisse and P. Roncin, Grazing incidence diffraction of kev helium atoms on a Ag(110) surface, *Phys. Rev. Lett.*, 2008, **101**, 177601.
- 90 M. Busch, A. Schüller, S. Wethekam and H. Winter, Fast atom diffraction at metal surface, *Surf. Sci.*, 2009, **603**(3), L23–L26.
- 91 P. Atkinson, M. Eddrief, V. H. Etgens, H. Khemliche, M. Debiossac, A. Momeni, M. Mulier, B. Lalmi and P. Roncin, Dynamic grazing incidence fast atom diffraction during molecular beam epitaxial growth of GaAs, *Appl. Phys. Lett.*, 2014, **105**(2), 021602.
- 92 T. Igel, R. Pfandzelter and H. Winter, Intensity oscillations in grazing scattering of fast He⁺ ions during heteroepitaxial growth of Cr on Fe(100), *EPL*, 1996, **35**(1), 67.
- 93 J. Seifert and H. Winter, In-situ monitoring of oxygen adsorption at Mo(112) surface via fast atom diffraction, *Surf. Sci.*, 2013, **610**, L1–L5.
- 94 A. Schüller, M. Busch, S. Wethekam and H. Winter, Fast atom diffraction from superstructures on a Fe(110) surface, *Phys. Rev. Lett.*, 2009, **102**, 017602.
- 95 J. Seifert, M. Busch, E. Meyer and H. Winter, Surface Structure of Alanine on Cu(110) Studied by Fast Atom Diffraction, *Phys. Rev. Lett.*, 2013, **111**(13), 137601.
- 96 J. Seifert, D. Blauth and H. Winter, Evidence for 2D-network structure of monolayer silica film on Mo(112), *Phys. Rev. Lett.*, 2009, **103**, 017601.
- 97 A. Zugarramurdi, M. Debiossac, P. Lunca-Popa, A. J. Mayne, A. Momeni, A. G. Borisov, Z. Mu, P. Roncin and H. Khemliche, Determination of the geometric corrugation of graphene on SiC(0001) by grazing incidence fast atom diffraction, *Appl. Phys. Lett.*, 2015, **106**(10), 101902.
- 98 J. R. Manson, Inelastic scattering from surfaces, *Phys. Rev. B: Condens. Matter Mater. Phys.*, 1991, **43**, 6924–6937.
- 99 P. Kraus, A. Tamtögl, M. Mayrhofer-Reinhartshuber, F. Apolloner, C. Gösweiner, S. Miret-Artés and W. Ernst, Surface structure of Bi(111) from helium atom scattering measurements. Inelastic close-coupling formalism, *J. Phys. Chem. C*, 2015, **119**(30), 17235.
- 100 A. Politano, A. R. Marino, D. Campi, D. Farías, R. Miranda and G. Chiarello, Elastic properties of a macroscopic graphene sample from phonon dispersion measurements, *Carbon*, 2012, **50**(13), 4903–4910.
- 101 B. S. Zhao, S. A. Schulz, S. A. Meek, G. Meijer and W. Schöllkopf, Quantum reflection of helium atom beams

- from a microstructured grating, *Phys. Rev. A: At., Mol., Opt. Phys.*, 2008, **78**, 010902.
- 102 F. Masson and J. Rabalais, Time of flight scattering and recoiling spectrometry (tof sars) analysis of Pt(110). 1. quantitative structural study of the clean (1x2) surface, *Surf. Sci.*, 1991, **253**(1–3), 245–257.
- 103 S. Lupone, S. Damoy, A. Husseen, N. Briand, M. Debiossac, S. Tall and P. Roncin, Note: A large open ratio, time, and position sensitive detector for time of flight measurements in uhv, *Rev. Sci. Instrum.*, 2015, **86**(12), 126115.
- 104 P. Roncin, Revisiting atomic collisions physics with highly charged ions: a tribute to Michel Barat, *J. Phys. B: At., Mol. Opt. Phys.*, 2020, **53**, 202001.
- 105 H. Winter, Collisions of atoms and ions with surfaces under grazing incidence, *Phys. Rep.*, 2002, **367**(5), 387–582.
- 106 L. Lavoine, P. Roncin and A. G. Borisov, 2021, in preparation.
- 107 L. Frisco and M. S. Gravielle, Thermal effects on helium scattering from LiF(001) at grazing incidence, Accepted to *Phys. Rev. A*.